Simulating waves and their interactions with a restrained ship using a non-hydrostatic wave-flow model

Dirk P. Rijnsdorp*, Marcel Zijlema

Environmental Fluid Mechanics Section, Faculty of Civil Engineering and Geosciences, Delft University of Technology, P.O. Box 5048, 2600 GA Delft, The Netherlands

Abstract

This paper presents a numerical model to simulate the evolution of waves and their interactions with a restrained ship that is moored in coastal waters. The model aims to be applicable at the scale of a harbour or coastal region, while accounting for the key physical processes that determine the hydrodynamic loads on the ship. Its methodology is based on the non-hydrostatic wave-flow model SWASH, which provides an efficient tool to simulate the nonlinear dynamics that govern the nearshore wave field. In this work, we propose a new numerical algorithm that accounts for the presence of a non-moving floating body, to resolve the wave impact on a restrained ship. The model is validated through comparisons with an analytic solution, a numerical solution, and two laboratory campaigns. The results of the model-data comparison demonstrate that the model captures the scattering of waves by a restrained body. Furthermore, it gives a reasonable prediction of the hydrodynamic loads that act on a restrained container ship for a range of wave conditions. Importantly, the model captures these dynamics efficiently, which demonstrates that it retains this favourable property of the non-hydrostatic approach when a floating body is included. The findings of this study suggest that the model provides a promising new alternative to simulate the nonlinear evolution of waves and their impact on a restrained ship at the scale of a realistic harbour or coastal region.

Keywords: moored ship, wave-ship interactions, wave scattering, hydrodynamic loads, non-hydrostatic, SWASH

1. Introduction

A ship that is moored in a harbour or coastal region is subject to the local wave field, which may cause the moored ship to move. When the motions of the ship become too large, ship operations may need to be terminated, resulting in undesired economic losses. Therefore, an accurate prediction of the local wave field, the hydrodynamic loads acting on the ship (the forces and moments), and the resulting ship motions are of vital importance to ensure safe and continuous operations of a moored ship.

---

*Corresponding author. Tel.: +31 15 278 5433.
Email address: d.p.rijnsdorp@tudelft.nl (Dirk P. Rijnsdorp)

Numerical models provide a valuable tool to predict the wave-induced response of a moored ship. Such a model should account for the interactions between the local wave field and the ship, such as the scattering of the waves by the ship, and the radiation of waves due to the ship motions (e.g., Newman, 1977). Furthermore, the model should account for the complex nearshore evolution of the waves as they propagate from relatively deep water to shallower water depths. This includes processes like shoaling, refraction, diffraction, wave breaking, and nonlinear interactions. The latter is especially relevant in the nearshore, as nonlinear wave effects like infragravity waves can cause significant ship motions (e.g., González-Marco et al., 2008; Sakakibara and Kubo, 2008; López and Iglesias, 2014). This highlights that an accurate description of the local nonlinear wave field is required when predicting the wave-induced response of a ship that is moored in coastal waters.

A variety of model techniques have been developed to simulate the interactions between waves and ships (see Bertram, 2012, for a concise overview). The first efforts to solve these interactions were based on potential flow theory (e.g., Korvin-Kroukovsky and Jacobs, 1957; Hess and Smith, 1962), in which the flow is assumed to be irrotational and inviscid. In this context, the Boundary Element Method (BEM) has been a popular method to solve the wave-ship interactions. Such models, which are also known as panel models, are applied in both offshore (e.g., Huijsmans et al., 2001; Newman, 2005; Zhao et al., 2011) and coastal waters (e.g., Van Oortmerssen, 1976; You and Faltinsen, 2015; Xiong et al., 2015) to predict the wave impact on floating bodies. More recently, potential flow models based on the Finite Element Method (FEM) have been developed to simulate similar interactions (e.g., Yan and Ma, 2007; Ma and Yan, 2009). Potential flow models based on the BEM and FEM share that they are not designed to simulate the evolution of waves at the scales of a coastal or harbour region. Consequently, they require information concerning the local wave field to predict the ship response based on an offshore wave climate

Furthermore, the assumption of potential flow is violated in the case of large wave impacts and significant ship motions (e.g., ship capsizing). In such extreme conditions, an alternative approach is desired to adequately simulate the ship response. With the increase of computational powers, various detailed Computational Fluid Dynamics (CFD) models have been developed that can resolve the turbulent flow field in the vicinity of a floating body. Examples include models that are based on the Reynolds-averaged Navier-Stokes (RANS) equations (e.g., Hadžić et al., 2005; Lin, 2007; Stern et al., 2013), and models based on the Smoothed Particle Hydrodynamics (SPH) method (e.g., Bouscasse et al., 2013; Ren et al., 2015). For instance, RANS models have been used to simulate the seakeeping of ships, including the turbulent wake of the ship and rotating propellers (e.g., Wilson et al., 2006; Mofidi and Carrica, 2014). However, computational limitations restrict the application of such highly detailed models to relatively small scales, spanning only a few wave lengths and wave periods.

To simulate both the evolution of waves and their interactions with ships, several authors combined a wave model with a model that accounts for the wave-ship interactions (e.g., Bingham, 2000; Jiang et al., 2002;

Van der Molen et al., 2006; Van der Molen and Wenneker, 2008; Dobrochinski, 2014). To our knowledge, the most advanced methodology that can solve this complex problem combined a phase resolving wave model (i.e., a Boussinesq or a non-hydrostatic wave model) with a panel model (Bingham, 2000; Van der Molen and Wenneker, 2008; Dobrochinski, 2014). In this approach, the wave model is first used to simulate the evolution of the waves as they propagate in coastal waters. The wave model does not account for the presence of the ship, and the computed wave field represents the waves that are not disturbed by the ship. Next, a panel model based on linear potential theory is used to compute the interactions between this undisturbed wave field and the ship. The advantage of such a coupled wave-panel model is that it combines a wave model that can resolve the nonlinear wave evolution from deep to shallow water at the scale of a harbour or coastal region, with a panel model that includes a detailed schematisation of the ship's hull to determine the wave-induced response. However, the assumption of linear potential flow restricts this approach to relatively mild wave conditions, when the wave non-linearity is small (i.e., $a/d \ll 1$ in shallow water, where a is the wave amplitude and d is the still water depth, Bingham, 2000). Moreover, the coupling of two models complicates the usage and maintenance of this methodology.

In this work, we pursue an alternative approach to simulate the evolution of waves and their impact on a ship that is moored in coastal waters. Our ultimate goal is to develop a single model to simulate the wave-induced response of a moored ship based on an offshore wave climate. The model aims to be applicable at the scales of a harbour or coastal region, while accounting for the relevant processes on both relatively large scale (the nonlinear wave transformation over a complex bathymetry) and on small scale (the wave-ship interactions). Our approach is based on the non-hydrostatic wave-flow model SWASH[1]. Recent studies have shown that non-hydrostatic wave-flow models like SWASH are capable of resolving the complex evolution of waves over sloping bottoms (e.g., Yamazaki et al., 2009; Ma et al., 2012; Cui et al., 2012). This includes the nonlinear wave dynamics in the surf zone (Smit et al., 2013, 2014), and the nearshore evolution of infragravity waves (e.g., Ma et al., 2014b; Rijnsdorp et al., 2014, 2015; De Bakker et al., 2016), which play a key role in the wave-induced response of a ship that is moored in shallow water. This paper presents the first crucial step towards the development of such a single model tool. To predict the wave-induced response of a moored ship, an accurate description of the local wave field and the hydrodynamic loads are of vital importance. In this work, we advance the capabilities of the SWASH model to resolve the interactions between the waves and a non-moving floating body. This allows the model to resolve the wave impact on a restrained ship, providing the basis for future developments to simulate the wave-induced motions of a moored ship.

In non-hydrostatic models like SWASH, a fractional step method is used to solve the RANS equations. In this approach, the pressure is decomposed into a hydrostatic and a non-hydrostatic part. First, a discrete

---

[1]Simulating <u>WA</u>ves till <u>SH</u>ore, available under the GNU GPL license at `http://swash.sourceforge.net/`.

free-surface equation is solved for the hydrostatic pressure (which determines the position of the free surface) to compute a provisional velocity field. In the subsequent step, the velocities are corrected after solving a Poisson equation for the non-hydrostatic pressure. One of the key properties of such models is their efficiency in simulating the nearshore wave dynamics due to the use of the Keller-Box scheme to discretise the non-hydrostatic pressure (e.g., Stelling and Zijlema, 2003).

In this work, we present a new numerical algorithm to account for the presence of a non-moving floating body in such a model (see §2). The inclusion of a floating body complicates the problem as the model has to account for the simultaneous occurrence of free-surface flow and the pressurised flow underneath the body. Following the approach of Casulli and Stelling (2013), we derived a free-surface equation that correctly describes the global continuity equation in both the free surface and the pressurised region. To ensure that the method is unconditionally stable with respect to the wave celerity (which is infinite in the pressurised region), our algorithm is based on the semi-implicit version of the SWASH model (e.g., Zijlema and Stelling, 2005). Furthermore, we used the first-order pressure projection method (e.g., Chorin, 1968), instead of the second-order pressure correction method (e.g., Van Kan, 1986) that is used in SWASH, to deal with the pressurised flow underneath the ship. However, to retain the second-order accuracy when simulating free-surface flows, the second-order projection method is used in regions where the flow is bounded by a free surface (e.g., Vitousek and Fringer, 2013).

To assess the capabilities of this approach, we validated the model for the interactions between waves and a restrained ship using a total of four test cases. The first two tests consider the scattering of waves by a rectangular pontoon in a two-dimensional vertical (2DV) domain. First, we validate the model using an analytic solution for the scattering of linear monochromatic waves (§3). The second test case is based on a numerical solution of the scattering of a solitary wave (§4). Following these 2DV tests, we consider two laboratory experiments that were conducted in a wave basin, to assess the model capabilities in a three-dimensional (3D) physical domain. The third test case focusses on the scattering of regular waves by a rectangular pontoon (§5). To gain insight in the model capabilities for a more realistic environment, the final test considers an experimental campaign in which a realistic ship model (a Panamax container ship) was subject to a range of wave conditions, including short-crested sea states (§6). Finally, we summarise and discuss our findings in §7.

2. Numerical Methodology

The numerical methodology of the model that was developed in this work is based on the non-hydrostatic wave-flow model SWASH (Zijlema et al., 2011). The governing equations of the model are the RANS equations for an incompressible fluid with a constant density. The model solves the layer-averaged RANS equations using a curvilinear coordinate framework for the two horizontal dimensions, and a terrain following

129 coordinate framework for the vertical dimension.

130 In the following, we present the numerical methodology that was adopted to account for the presence of
131 a non-moving floating body. For the sake of clarity, we present our approach in its simplest form, without
132 loss of generality. We present the numerical approach in a Cartesian framework and for one horizontal
133 dimension. This relatively simple presentation of the modelling framework includes the numerical details
134 that are relevant for including a floating body in the numerical domain. Although porous structures are
135 included in the simulations of one of the test cases, we do not discuss their numerical discretisation as this
136 is not the focus of this study (see Appendix A for a brief description of its implementation).

2.1. Governing equations

138 We consider a two-dimensional domain that is bounded in the vertical by an interface at the top and at
139 the bottom (see Fig. 1). At the top interface, the domain is bounded by either a free surface $z = \zeta(x,t)$, or
140 a rigid non-moving floating body $z = -S(x)$, where t is time, x and z are the Cartesian coordinates, and
141 $z = 0$ is the still water level. At the bottom, the domain is bounded by a fixed bed, $z = -d(x)$. In this
142 domain, we can distinguish between two subdomains: an outer domain where the flow is bounded by a free
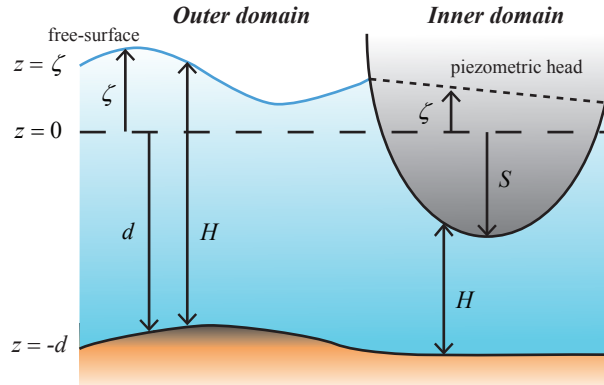143 surface, and an inner domain where the flow is pressurised.

Figure 1: Sketch of the two-dimensional domain, including a free surface, a floating body, and a fixed bed.

144 In this framework, the governing equations read,

$$\frac{\partial u}{\partial x} \quad + \quad \frac{\partial w}{\partial z} = 0, \tag{1}$$

$$\frac{\partial u}{\partial t} \quad + \quad \frac{\partial uu}{\partial x} + \frac{\partial wu}{\partial z} = -g\frac{\partial \zeta}{\partial x} - \frac{\partial p}{\partial x} + \frac{\partial \tau_{xx}}{\partial x} + \frac{\partial \tau_{xz}}{\partial z}, \tag{2}$$

$$\frac{\partial w}{\partial t} \quad + \quad \frac{\partial uw}{\partial x} + \frac{\partial ww}{\partial z} = -\frac{\partial p}{\partial z} + \frac{\partial \tau_{zx}}{\partial x} + \frac{\partial \tau_{zz}}{\partial z}, \tag{3}$$

148 where $u(x,z,t)$ is the velocity in x direction, $w(x,z,t)$ is the velocity in z direction, g is the gravitational
149 acceleration, $\tau(x,z,t)$ represents the turbulent stresses, $p(x,z,t)$ is the non-hydrostatic pressure (normalised

5

by a reference density), and $\zeta(x,t)$ is the piezometric head (which is equivalent to the free surface in the outer domain, see Fig. 1). At the top and bottom interfaces, the following kinematic boundary conditions apply,

$$w|_{z=\zeta} = \frac{\partial \zeta}{\partial t} + u\frac{\partial \zeta}{\partial x}, \tag{4}$$

$$w|_{z=-S} = -u\frac{\partial S}{\partial x}, \tag{5}$$

$$w|_{z=-d} = -u\frac{\partial d}{\partial x}. \tag{6}$$

At the bottom, we approximate the effect of bottom friction using a quadratic friction law,

$$\tau_{xz}|_{z=-d} = c_f\frac{U|U|}{H}, \tag{7}$$

where c_f is a dimensionless friction coefficient, H is the total water depth, and $U \left(= \frac{1}{H}\int u\,\mathrm{d}z\right)$ is the depth-averaged velocity. In this study, we computed c_f using the Manning-Strickler formulation ($c_f = gn^2/H^{1/3}$, where n is the Manning roughness coefficient). The turbulent stresses are evaluated using a turbulent viscosity approximation (e.g., $\tau_{xx} = \nu_h\frac{\partial u}{\partial x}$ in which ν_h is the horizontal eddy viscosity, and $\tau_{xz} = \nu_v\frac{\partial u}{\partial z}$ in which ν_v is the vertical eddy viscosity). In a 3D framework, the horizontal viscosities are estimated using a Smagorinsky-type formulation (Smagorinsky, 1963). In this work, the model is applied with a coarse vertical resolution (2 layers) which implies that it does not fully resolve the vertical flow profile. To account for some vertical mixing nonetheless, and to spread the effect of bottom friction over the vertical, the vertical viscosity ν_v was set at a constant value of 10^{-4} m^{2}s^{-1}.
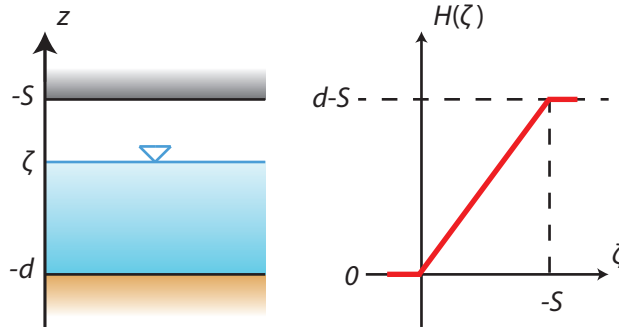

Figure 2: Piecewise linear function of the total water depth H, that is bounded by a fixed bottom ($z = -d$) and a floating body ($z = -S$).

To close the set of equations, we derive an extra equation to determine the piezometric head. Integrating the continuity equation (1) from the bottom to the free surface and applying the relevant kinematic boundary conditions (4 and 6) yields the following global-continuity equation in the outer domain,

$$\frac{\partial \zeta}{\partial t} + \frac{\partial}{\partial x}\int_{-d}^{\zeta} u\mathrm{d}z = \frac{\partial \zeta}{\partial t} + \frac{\partial HU}{\partial x} = 0,$$

6

where $H = d + \zeta$ is the water depth in the outer domain. This equation governs the position of the free surface in the outer domain, where the waves are dispersive. However, when a floating body is included in the domain, a different equation applies in the pressurised region. Integrating Eq. (1) with the relevant kinematic boundary conditions (5,6) yields the following equation,

$$\frac{\partial}{\partial x} \int\limits_{-d}^{-S} u \, \mathrm{d}z = \frac{\partial HU}{\partial x} = 0,$$

where $H = d - S$ is the water depth in the inner domain. This steady-state equation determines the piezometric head in the pressured region. With the present assumptions of an incompressible fluid and a rigid floating body, this equation implies that the celerity is infinite underneath the ship. Consequently, perturbations in the flow and pressure field are spread instantly over the entire inner domain.

Following the approach of Casulli and Stelling (2013), these two global continuity equations are recast into a single equation by defining the total water depth as a piecewise linear function of the piezometric head, $H(\zeta) = \max\left(0, d + \min\left(-S, \zeta\right)\right)$. With this formulation, the water depth has a minimal value of zero, and increases linearly as a function of ζ, with an upper bound equal to the level of the floating body (illustrated in Fig. 2). With this definition of the water depth, the two global continuity equations are combined into,

$$\frac{\partial \max\left(-d, \min\left(-S, \zeta\right)\right)}{\partial t} + \frac{\partial HU}{\partial x} = 0. \tag{8}$$

This single equation captures the nature of the flow in the outer and inner domain. This implies that the resulting model accounts for the finite celerity in the outer domain (where waves are dispersive), and the infinite celerity in the inner domain where the flow is pressurised. Furthermore, a pressurised cell can become a free surface cell, and vice versa. This allows the model to account for the wetting and drying of the ship as the water moves up and down the hull.

2.2. Spatial and temporal discretisation

The governing equations are discretised on a structured grid with a fixed number of layers K between the top and bottom interface, where $k = 1$ is the bottom layer, and $k = K$ is the top layer. The resulting grid has a spatially varying layer thickness of $h_k = H/K$, and a constant width Δx. A staggered grid is used to arrange the variables: the piezometric head is located at a cell centre, the u velocities are located at the centre the horizontal cell faces and the w velocities are located at the centre of the vertical cell faces (see Fig. 3). In the outer domain, the non-hydrostatic pressure variables are located at a vertical cell face following the Keller-Box scheme (Lam and Simpson, 1976). Compared to the traditional cell centred arrangement (e.g., Stansby and Zhou, 1998; Casulli and Stelling, 1998), this cell face arrangement significantly improves the dispersive properties of the model (e.g., Stelling and Zijlema, 2003; Smit et al., 2014). For typical coastal and harbour applications, two layers are generally sufficient to resolve the dispersion of the wave field. In the simulations of this paper, two vertical layers were used as well.
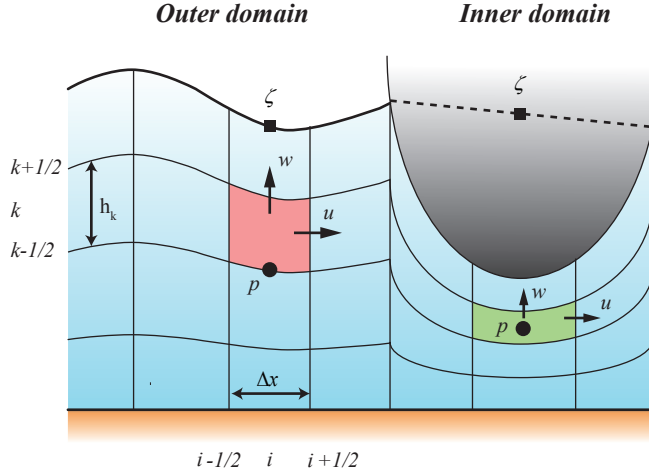
Figure 3: Horizontal and vertical grid definition, and the staggered variable arrangement on grid. A cell with its centre at i, k is bounded by a top $(k + 1/2)$ and bottom interface $(k - 1/2)$, and the left $(i - 1/2)$ and right $(i + 1/2)$ grid interfaces. The variable arrangement is depicted for the outer domain (illustrated in the red control volume) and the inner domain (illustrated in the green control volume).

In the inner domain, the piezometric head and velocity variables are arranged in a similar fashion. However, the non-hydrostatic pressure variables are arranged using the cell centred arrangement instead of the Keller-Box scheme. We adopt this arrangement as the application of the Keller-Box scheme is not advantageous in the inner domain where the celerity is infinite. In addition, the centred arrangement allows for an easier implementation, and results in a smaller stencil of the Poisson equation, which will become apparent in the following (e.g., Eq. (14)).

A variable which is required at a location where it is not known is interpolated or extrapolated from its surrounding variables. In both domains, these techniques follow the methodology of SWASH. Details regarding the various types of interpolation used in SWASH (e.g., linear interpolation, upwind approximations, and flux limiters) can be found in Zijlema and Stelling (2005, 2008), and Zijlema et al. (2011). In the following, variables that are computed using (bi)linear interpolation or extrapolation are denoted with an overline, including the direction in which it takes place. For example, a layer thickness at the cell face $i + 1/2$ that is computed using linear interpolation in x direction is written as $\overline{h_{i+1/2,k}}^x$. Variables that are interpolated using upwind approximations, or flux limiters are denoted with a hat (e.g., $\hat{H}_{i+1/2}$). To achieve second-order accuracy in space, and to avoid undesired oscillations near sharp gradients, we use the MUSCL limiter (Van Leer, 1979) to determine the water depth and layer thickness at a horizontal cell face (e.g., Zijlema et al., 2011). Note that the water depth follows from $H = d - S$ if a cell is located in the inner domain. Here, the water depth and the layer thickness at a cell face can be directly computed from the position of the bottom and the ship, and do not require interpolation.

8

To simulate the simultaneous occurrence of free surface and pressurised flows, the numerical method must be unconditionally stable with respect to the celerity, which is infinite in the pressurised region (e.g., Casulli and Stelling, 2013). For this purpose, we use an (semi) implicit method to discretise the velocities in the global continuity equation (8) and the piezometric head and the non-hydrostatic pressure in the momentum equations (2-3). The advective and turbulent stress terms in the momentum equations (2-3) are discretised using the same methods as in SWASH. As such, the vertical advective and turbulent stress terms are discretised using the semi-implicit θ-scheme (with $\theta = 1/2$), to prevent a time step restriction when the water depth becomes small (e.g., in the case of flooding and drying at a beach). Explicit schemes are used to discretise the horizontal advective (the second-order accurate MacCormack scheme) and the turbulent stress terms (the first-order accurate explicit Euler scheme). In space, the turbulent terms are discretised using (second-order) central differences. For the spatial discretisation of the advective terms, various numerical techniques can be used in SWASH (e.g., first-order upwind, flux limiters, and central differences). In this work, the advective terms in the $u-$momentum equation are discretised using the MUSCL limiter. In the $w-$momentum equation, the horizontal advective terms are discretised using the second-order BDF scheme, and the vertical term is discretised using the first-order upwind scheme.

In the following, we present the discretised versions of the layer-averaged equations, and the solution algorithm that we adopted to include a floating body. To improve the readability of the paper, we focus on the aspects that are affected by including a floating body in the domain. As the inclusion of the body does not affect the integration of the equations over a layer, we omit their details as they have been extensively treated before (Stelling and Zijlema, 2003; Zijlema and Stelling, 2005). For the same reason, we do not present the discretisation of the advective and turbulent stress terms. Details regarding their discretisation can be found in Zijlema and Stelling (2005, 2008) and Zijlema et al. (2011).

2.2.1. Continuity equations

The global continuity equation (8) is discretised in time using the θ-method. For brevity, we will write the semi-implicit terms that arise due to this method for some variable ϕ as $\phi^{n+\theta} = \theta\phi^{n+1} + (1-\theta)\phi^n$, in which n indicates the time level ($t^n = n\Delta t$, where Δt is a fixed time step) and θ is an implicitness factor (with an allowable range of $1/2 \leq \theta \leq 1$). With $\theta = 1$ the θ-method is equivalent to the first-order accurate implicit Euler method, and with $\theta = 1/2$ it is equivalent to the second-order Crank Nicholson method. A global mass conserving discretisation of Eq. (8) is given by,

$$\frac{\max\left(-d_i, \min\left(-S_i, \zeta_i^{n+1}\right)\right) - \max\left(-d_i, \min\left(-S_i, \zeta_i^n\right)\right)}{\Delta t} + \frac{\hat{H}_{i+1/2}^n U_{i+1/2}^{n+\theta_{i+1/2}} - \hat{H}_{i-1/2}^n U_{i-1/2}^{n+\theta_{i-1/2}}}{\Delta x} = 0, \quad (9)$$

in which U is the approximated depth-averaged velocity ($U = 1/H \sum_{k=1}^{K} h_k u_k$, where u_k is the layer-averaged $u-$velocity). In this work, a spatially varying $\theta_{i\pm1/2}$ parameter is adopted to account for the different flow regimes in the outer and inner domain. To compute the steady-state solution of Eq. (9) when the flow

9

is pressurised, the value of $\theta_{i\pm1/2}$ is set at 1 when a horizontal grid interface $i\pm1/2$ is located in the inner domain. If an interface is located in the outer domain, $\theta_{i\pm1/2} = 1/2$ to prevent numerical wave damping.

A local mass conserving discretisation of the local continuity equation (1) is given by,

$$\frac{\overline{h^n_{i+1/2,k}}^x u^{n+1}_{i+1/2,k} - \overline{h^n_{i-1/2,k}}^x u^{n+1}_{i-1/2,k}}{\Delta x} + w^{n+1}_{i,k+1/2} - w^{n+1}_{i,k-1/2}$$
$$- \overline{u^{n+1}_{i,k+1/2}}^{xz} \frac{z^n_{i+1/2,k+1/2} - z^n_{i-1/2,k+1/2}}{\Delta x} + \overline{u^{n+1}_{i,k-1/2}}^{xz} \frac{z^n_{i+1/2,k-1/2} - z^n_{i-1/2,k-1/2}}{\Delta x} = 0, \tag{10}$$

in which $z_{k\pm1/2}$ represent the vertical position of the interfaces at the top $(z_{k+1/2})$ and bottom $(z_{k-1/2})$ of a layer.

2.2.2. Momentum equations

The layer-averaged version of the u-momentum equation (2) is discretised as,

$$\frac{u^{n+1}_{i+1/2,k} - u^n_{i+1/2,k}}{\Delta t} = -g\frac{\zeta^{n+\theta_{i+1/2}}_{i+1} - \zeta^{n+\theta_{i+1/2}}_i}{\Delta x} - Pu^{n+1}_{i+1/2,k}, \tag{11}$$

where $Pu^{n+1}_{i+1/2,k}$ represents the discretisation of the non-hydrostatic pressure term. For brevity, we omit details regarding the discretisation of the advective and turbulent terms in this momentum equation. For the time integration of the piezometric head gradient, the θ-method is used with a spatially varying $\theta_{i\pm1/2}$ parameter. Similar to the global continuity equation, the value of this parameter is set depending on the location of the grid interface $i\pm1/2$, that is, $\theta_{i\pm1/2} = 1/2$ in the outer domain and $\theta_{\pm1/2} = 1$ in the inner domain.

The layer-averaged non-hydrostatic pressure term is evaluated as,

$$Pu_k = \frac{1}{h_k}\int_{z_{k-1/2}}^{z_{k+1/2}} \frac{\partial p}{\partial x}\mathrm{d}z = \frac{1}{h_k}\left(\frac{\partial p_k h_k}{\partial x} - p_{k+1/2}\frac{\partial z_{k+1/2}}{\partial x} + p_{k-1/2}\frac{\partial z_{k-1/2}}{\partial x}\right).$$

Discretising this term yields different expressions in the outer and inner domain due to the differences in the arrangement of the non-hydrostatic pressure variable (Fig. 3). In discretised form, $Pu^{n+1}_{i+1/2,k}$ reads,

$$Pu^{n+1}_{i+1/2,k} = \begin{cases} \dfrac{1}{\overline{h^n_{i+1/2,k}}^x}\left[\dfrac{\overline{p^{n+1}_{i+1,k}}^z h^n_{i+1,k} - \overline{p^{n+1}_{i,k}}^z h^n_{i,k}}{\Delta x}\right. \\[2ex] \qquad\qquad - \overline{p^{n+1}_{i+1/2,k+1/2}}^x \dfrac{z^n_{i+1,k+1/2} - z^n_{i,k+1/2}}{\Delta x} \qquad \text{(Outer domain)}, \\[2ex] \qquad\qquad \left.+ \overline{p^{n+1}_{i+1/2,k-1/2}}^x \dfrac{z^n_{i+1,k-1/2} - z^n_{i,k-1/2}}{\Delta x}\right] \\[3ex] \dfrac{1}{\overline{h^n_{i+1/2,k}}^x}\left[\dfrac{p^{n+1}_{i+1,k} h^n_{i+1,k} - p^{n+1}_{i,k} h^n_{i,k}}{\Delta x}\right. \\[2ex] \qquad\qquad - \overline{p^{n+1}_{i+1/2,k+1/2}}^{xz} \dfrac{z^n_{i+1,k+1/2} - z^n_{i,k+1/2}}{\Delta x} \qquad \text{(Inner domain)}. \\[2ex] \qquad\qquad \left.+ \overline{p^{n+1}_{i+1/2,k-1/2}}^{xz} \dfrac{z^n_{i+1,k-1/2} - z^n_{i,k-1/2}}{\Delta x}\right] \end{cases} \tag{12}$$

10

This discretisation introduces virtual points in both the outer and inner domain. For example, virtual points are located at the vertical cell faces in the inner domain, which are interpolated or extrapolated from the surrounding pressure variables (e.g., $\overline{p_{i+1/2,k+1/2}^{n+1}}^{xz}$). Note that we take advantage of the pressure boundary condition at the free surface in the outer domain (i.e., $p|_{z=\zeta} = 0$), to prescribe the pressure variables at the free surface.

The layer-averaged version of the w-momentum equation (3) is discretised as,

$$\frac{w_{i,k+1/2}^{n+1} - w_{i,k+1/2}^{n}}{\Delta t} = -Pw_{i,k+1/2}^{n+1}, \tag{13}$$

where $Pw_{i,k+1/2}^{n+1}$ represents the discretisation of the non-hydrostatic pressure term. In this equation, we omit details regarding the advective and turbulent terms for brevity. In the outer domain, Eq. (13) applies at all interfaces except for the bottom, where the kinematic boundary condition (6) applies. In the inner domain, Eq. (13) only applies at the internal interfaces, and the kinematic boundary conditions apply at the top (5) and bottom interface (6).

Similar to the u-momentum equation, the discretised form of the non-hydrostatic pressure term is different in the outer and inner domain. In the outer domain, the non-hydrostatic pressure term, $Pw_{k+1/2} = \int_{z_k}^{z_{k+1}} \frac{\partial p}{\partial z} dz$, is evaluated using the Keller-Box scheme (Lam and Simpson, 1976). In this method, the non-hydrostatic pressure gradient is evaluated as the arithmetic average of the gradients at the vertical cell faces,

$$\frac{\partial p_k}{\partial z} = \frac{1}{2}\frac{\partial p_{k+1/2}}{\partial z} + \frac{1}{2}\frac{\partial p_{k-1/2}}{\partial z}.$$

With this expression, and following a straightforward evaluation of the $\frac{\partial p_k}{\partial z}$ term, we derive an expression for the gradient at the top cell interface $\frac{\partial p_{k+1/2}}{\partial z}$,

$$\frac{1}{2}\frac{\partial p_{k+1/2}}{\partial z} + \frac{1}{2}\frac{\partial p_{k-1/2}}{\partial z} = \frac{\partial p_k}{\partial z} \approx \frac{p_{k+1/2} - p_{k-1/2}}{h_k} \rightarrow \frac{\partial p_{k+1/2}}{\partial z} = 2\frac{p_{k+1/2} - p_{k-1/2}}{h_k} - \frac{\partial p_{k-1/2}}{\partial z}.$$

The gradient at one interface lower, $\frac{\partial p_{k-1/2}}{\partial z}$, is evaluated similarly. A subsequent substitution of these gradient terms into $Pw_{k+1/2}$ results in the following expression,

$$Pw_{k+1/2} = \sum_{m=0}^{k-1}\left[(-1)^m 2\frac{p_{k+1/2-m} - p_{k-1/2-m}}{h_{k-m}}\right] + (-1)^k\frac{\partial p_{1/2}}{\partial z}.$$

To close this expression, the vertical gradient of the non-hydrostatic pressure needs to be evaluated at the bottom (i.e., $\frac{\partial p_{1/2}}{\partial z}$). This term is neglected in this work as its contribution is zero when the bottom is flat, which is the case in the simulations of this study.

In the inner domain, we approximate the non-hydrostatic pressure term in a different manner,

$$Pw_{k+1/2} = \int_{z_k}^{z_{k+1}} \frac{\partial p}{\partial z}\mathrm{d}z = \frac{p_{k+1} - p_k}{\overline{h_{k+1/2}}^z}.$$

11

In conclusion, the discretised form of $Pw^{n+1}_{i,k+^1/_2}$ reads,

$$
Pw^{n+1}_{i,k+^1/_2} = \begin{cases} \displaystyle\sum_{m=0}^{k-1}\left[(-1)^m\, 2\frac{p^{n+1}_{i,k+^1/_2-m} - p^{n+1}_{i,k-^1/_2-m}}{h^n_{i,k-m}}\right] & \text{(Outer domain)}, \\[3mm] \dfrac{p^{n+1}_{i,k+1} - p^{n+1}_{i,k}}{\overline{h}^z_{i,k+^1/_2}} & \text{(Inner domain)}. \end{cases}
\tag{14}
$$

In the outer domain, this equation implies that Eq. (13) depends on all pressure variables that are located at, and below the interface of interest. In contrast, this equation only depends on the two surrounding pressure variables when a face is located in the inner domain.

2.3. Solution procedure

We employ a fractional step method that is known as the pressure projection method (e.g., Chorin, 1968) to solve the system of discretised equations. With this method, the time integration from n to $n+1$ is split into two steps. In the first step (or hydrostatic step), a provisional velocity field (u^*) and the piezometric head ζ^{n+1} are computed using a reduced number of terms in the momentum equations (11,13). In the second step (or non-hydrostatic step), the non-hydrostatic pressure p^{n+1} and the velocity field u^{n+1} and w^{n+1} are computed. Within the present framework, this fractional step procedure implies that the horizontal momentum equation (11) is solved in two steps. First, a provisional $u-$velocity is computed in the hydrostatic step,

$$
u^*_{i+^1/_2,k} = u^n_{i+^1/_2,k} - g\frac{\Delta t}{\Delta x}\left(\zeta^{n+\theta_{i+1/2}}_{i+1} - \zeta^{n+\theta_{i+1/2}}_i\right).
\tag{15}
$$

Subsequently, the u velocity at $n+1$ is computed in the non-hydrostatic step,

$$
u^{n+1}_{i+^1/_2,k} = u^*_{i+^1/_2,k} - \Delta t Pu^{n+1}_{i+^1/_2,k}.
\tag{16}
$$

2.3.1. Hydrostatic step

In the hydrostatic step, the global continuity equation (9) is solved to compute ζ^{n+1}. For this purpose, the horizontal momentum equation (16) is substituted into Eq. (9), which yields an implicit equation for the unknown ζ^{n+1}. In this work, we use a predictor-corrector technique to solve this implicit equation. With this technique, the computation of the provisional horizontal velocity field u^* (15) is divided into two steps. First, we predict an estimate of u^* based on the piezometric head at the previous time step,

$$
u^{**}_{i+^1/_2,k} = u^n_{i+^1/_2,k} - g\frac{\Delta t}{\Delta x}\left(\zeta^n_{i+1} - \zeta^n_i\right).
\tag{17}
$$

Subsequently, the provisional velocity field can be computed based on the piezometric head correction $\Delta\zeta\left(=\zeta^{n+1} - \zeta^n\right)$,

$$
u^*_{i+^1/_2,k} = u^{**}_{i+^1/_2,k} - \theta_{i+^1/_2}g\frac{\Delta t}{\Delta x}\left(\Delta\zeta_{i+1} - \Delta\zeta_i\right).
\tag{18}
$$

12

To solve this equation, the piezometric head correction needs to be computed first. Substituting the equations for u^{n+1} (16) and u^* (18) in the global continuity equation (9) yields an implicit equation for $\Delta\zeta$,

$$
\begin{aligned}
\max\left(-d_i - \zeta_i^n, \min\left(-S_i - \zeta_i^n, \Delta\zeta_i\right)\right) &- g\frac{\Delta t^2}{\Delta x^2}\left[\theta_{i+1/2}^2 \hat{H}_{i+1/2}^n \left(\Delta\zeta_{i+1} - \Delta\zeta_i\right) - \theta_{i-1/2}^2 \hat{H}_{i-1/2}^n \left(\Delta\zeta_i - \Delta\zeta_{i-1}\right)\right] \\
&= \max\left(-d_i - \zeta_i^n, \min\left(-S_i - \zeta_i^n, 0\right)\right) \\
&\quad - \frac{\Delta t}{\Delta x}\left[\hat{H}_{i+1/2}^n \left(\theta_{i+1/2}U_{i+1/2}^{**} + (1-\theta_{i+1/2})U_{i+1/2}^n\right) - \hat{H}_{i-1/2}^n \left(\theta_{i-1/2}U_{i-1/2}^{**} + (1-\theta_{i-1/2})U_{i-1/2}^n\right)\right] \\
&\quad + \sum_{k=1}^{K} \frac{\Delta t^2}{\Delta x}\left(\beta_{i+1/2}\theta_{i+1/2}\overline{h_{i+1/2,k}^n}^x Pu_{i+1/2,k}^{n+1} - \beta_{i-1/2}\theta_{i-1/2}\overline{h_{i-1/2,k}^n}^x Pu_{i-1/2,k}^{n+1}\right).
\end{aligned}
$$

$$(19)$$

This implicit equation represents a (positive definite and symmetric) tridiagonal piecewise-linear system of equations for $\Delta\zeta$, which is solved using the Newton-type iterative method of Brugnano and Casulli (2009) in combination with a tridiagonal matrix algorithm[2]. The parameter β indicates if the contribution of p^{n+1} is included ($\beta = 1$) or excluded ($\beta = 0$) in the global continuity equation. If $\beta = 1$ in Eq. (19), the temporal accuracy of the pressure projection method is second-order in simulating free-surface flows, whereas the method is first-order accurate if $\beta = 0$ (e.g., Vitousek and Fringer, 2013). Similar to $\theta_{i\pm1/2}$, the parameter $\beta_{i\pm1/2}$ can be varied in the domain, which will be discussed in §2.3.3. If $\beta_{i\pm1/2} = 1$ in any of the cells, Eq. (19) cannot be directly solved as the contribution of p^{n+1} in Pu^{n+1} is not yet known. To include this contribution, several iterations over the hydrostatic and non-hydrostatic steps are required.

2.3.2. Non-hydrostatic step

In the non-hydrostatic step, the velocity field at $n+1$ is computed based on the non-hydrostatic pressure at $n+1$. The u^{n+1} velocity is computed following Eq. (16), and w^{n+1} is computed as,

$$
w_{i,k+1/2}^{n+1} = w_{i,k+1/2}^n - \Delta t P w_{i,k+1/2}^{n+1}. \tag{20}
$$

To solve these equations, p^{n+1} is first computed based on the local continuity equation (10). Substituting the momentum equations and the relevant kinematic boundary conditions in Eq. (10) yields a Poisson equation for p^{n+1}. Fig. 4 illustrates the locations of the unknowns and the stencil of the non-hydrostatic pressure in the outer and inner domain for a model with two vertical layers. The Poisson equation (which is asymmetric and not positive definite) is solved using a preconditioned BiCGSTAB solver (e.g., Barrett et al., 1994; Zijlema and Stelling, 2005).

2.3.3. Solution algorithm

The solution algorithm can be summarised as follows,

---

[2]In the case of two horizontal dimensions, the system is pentadiagonal and solved using a preconditioned conjugate gradient method (e.g., Barrett et al., 1994).

1. Start the computation with ζ^n, u^n, w^n, p^n, from the initial conditions or from the previous time step.

2. **Hydrostatic step**

   (a) Solve Eq. (17) to compute the estimate of the provisional horizontal velocity (u^{**}).

   (b) Solve the global continuity equation (19) to compute the piezometric head correction ($\Delta\zeta$).

   (c) Solve Eq. (18) to compute the provisional horizontal velocity field (u^*), which satisfies the global continuity equation.

3. **Non hydrostatic step**

   (a) Solve the Poisson equation resulting from the local continuity equation (10) to compute the non-hydrostatic pressure at the next time step (p^{n+1}).

   (b) If the non-hydrostatic pressure is included in the hydrostatic step ($\beta = 1$), return to step 2b and repeat until convergence is reached.

4. Solve Eq. (16) and Eq. (20) to compute the divergence-free velocity field (u^{n+1}, and w^{n+1}), and advance the computation to the next time step.

This algorithm differs from the conventional SWASH model, which uses the explicit leapfrog scheme or the semi-implicit θ-method in combination with the pressure correction method of Van Kan (1986) to solve the layer-averaged RANS equations. However, to simulate the simultaneous occurrence of free surface and pressurised flows, the algorithm presented in this work is based on the semi-implicit version of the SWASH model as explicit schemes are not suited to simulate pressurised flows (e.g., Casulli and Stelling, 2013). Furthermore, we implemented a spatially varying implicitness parameter of the θ scheme, with $\theta = 1$ in the inner domain and $\theta = 1/2$ in the outer domain. This allows the model to compute the steady-state solution of the global continuity equation in the inner domain, and at the same time it prevents undesired numerical wave damping in the outer domain.
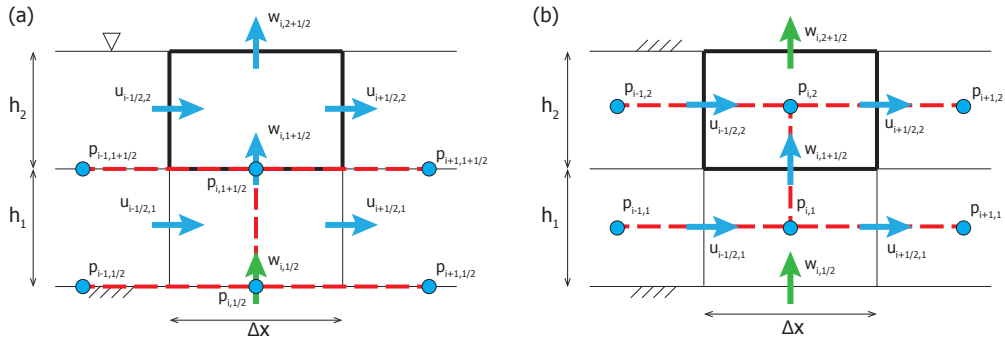

Figure 4: The locations of the unknowns, and the stencil of the non-hydrostatic pressure in the outer domain (a) and in the inner domain (b) for a two layer model. The thick black lines indicate the control volume of the local continuity equation. Green velocities are computed using the kinematic boundary condition, and blue velocities are computed using the momentum equations. The dashed red line indicates the stencil of the non-hydrostatic pressure.

14

377   The nature of the flow regime in the pressurised region also implies the use of the first-order accurate
378   pressure projection method ($\beta = 0$ in Eq. (19)), instead of the second-order accurate pressure correction
379   method. Note that the main difference between the pressure projection and pressure correction method is
380   the inclusion of an explicit non-hydrostatic pressure contribution in the hydrostatic step (see Stelling and
381   Zijlema, 2003, for more details). The disadvantage of the first-order scheme is that it introduces a significant
382   amount of wave damping in the outer domain. To retain the second-order accuracy in the outer domain and
383   to prevent this damping (e.g., Vitousek and Fringer, 2013), the non-hydrostatic pressure contribution was
384   included in the global continuity equation when a cell face is located in the outer domain (i.e., $\beta_{i\pm 1/2} = 1$ in
385   Eq. (19)).

2.4. Computation of hydrodynamic forces and moments

387   The resulting numerical model provides the flow and pressure field in the numerical domain, while
388   accounting for the presence of the floating body. The resulting hydrodynamic forces that act on the body
389   are found by integrating the total pressure over the wet surface of the body,

$$\mathbf{F} = \iint_{\mathcal{H}} P\mathbf{n} \, d\mathcal{H},$$

391   where $\mathbf{F} = (F_x, F_y, F_z)$, P is the total pressure (i.e., the combined hydrostatic and non-hydrostatic pressure),
392    $\mathcal{H}$ represents the wet surface of the body, and $\mathbf{n}$ is the unit vector normal to the body surface. The individual
393   components of $\mathbf{F}$ are known as the surge force (F_x), the sway force (F_y), and the heave force (F_z). The
394   moments around the centre of gravity of the body are computed as,

$$\mathbf{M} = \iint_{\mathcal{H}} (\mathbf{r} - \mathbf{r}_c) P\mathbf{n} \, d\mathcal{H},$$

396   where $\mathbf{M} = (M_x, M_y, M_z)$, $\mathbf{r}$ is the position vector of the pressure acting on the body surface, and $\mathbf{r}_c$ is the
397   position vector of the centre of gravity of the body. The individual components of $\mathbf{M}$ are known as the roll
398   moment (M_x), the pitch moment (M_y), and the yaw moment (M_z).

3. Scattering of linear monochromatic waves by a pontoon

400   We consider the interaction between linear monochromatic waves and a non-moving pontoon that is
401   located in water of constant depth (see Fig. 5 for the geometry and the dimensions of the pontoon). For
402   such a 2DV set-up, Cointe et al. (1991) presented an analytic solution of the linearised potential flow problem.
403   To asses the model capabilities for this problem, model results are compared with the analytic solution for
404   the (partial) reflection and transmission of the waves, and for the hydrodynamic loads that act on the body.
405   A comparison is made for a series of monochromatic waves, with periods varying between 1 to 5 s and a
406   constant small wave steepness ($a/L = 1\times 10^{-5}$, where a is the wave amplitude and L is the wave length).
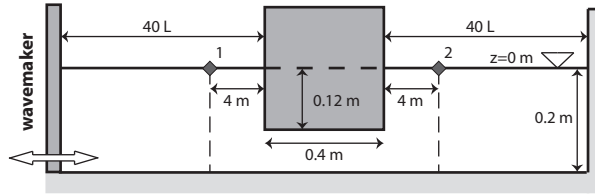
Figure 5: Sketch of the numerical set-up, including the geometry and dimensions of the pontoon. Note that the sketch is not at scale. The diamonds markers at the still water level indicate the output locations of the numerical model. These locations were positioned at a distance of 20 water depths away from the body (= 4 m), to minimise the effect of evanescent modes (which decay exponentially away from the pontoon).

In the analytic solution of Cointe et al. (1991), the domain is divided in three sub-domains (up wave, down wave and below the pontoon), in which the velocity potential is expressed by the appropriate eigenfunction expansions. These eigenfunction expansions consist of a single propagating wave mode and an infinite series of evanescent modes. In contrast with a propagating wave, evanescent modes exhibit an exponential behaviour in the horizontal plane, and a sinusoidal variation in the vertical. They are primarily important near sudden changes in the water depth, like the interfaces between the sub-domains. At these interfaces, they are necessary to match the different solutions in the sub-domains. Matching the eigenfunctions and their horizontal derivatives at the two interfaces between the three sub-domains, and truncating them at a certain number of terms, yields an algebraic system of equations for the unknown velocity potential. This system was solved using the Symbolic Toolbox of Matlab. For the wave conditions considered in this work, we found that the analytic solution converged when 21 terms were included in the eigenfunction expansions (not shown).

Fig. 5 illustrates the numerical set-up that was used in SWASH to reproduce this test case. A relatively large numerical domain (spanning more than 80 wave lengths) was used to prevent adverse effects on the analysis of wave reflections at the wavemaker and the vertical wall at the end of the domain. In the absence of such reflections, the predicted wave signal at sensor 2 represents a transmitted wave. Furthermore, as the wave conditions are linear, the signal at sensor 1 can be decomposed in an incident and reflected wave component. At this sensor, the incident signal was computed based on a simulation that excluded the floating body. Subsequently, the reflected signal was computed by taking the difference between the total signal and the incident signal at sensor 1. With this model set-up, the reflection and transmission coefficients were computed based on stationary reflected, transmitted, and reflected wave signals with a duration of at least 25 wave periods.

The temporal and grid resolution that was used in the SWASH simulations is based on the wave characteristics. The number of vertical layers was chosen based on the normalised water depth kd (in which k is the wave number), which determines the dispersive properties of the waves. In this test case, the kd values

ranged between $0.15 - 1$. For this range, two vertical layers are sufficient to resolve the wave dispersion (e.g., Zijlema et al., 2011; Smit et al., 2014). The horizontal grid resolution was set at 100 points per wave length (resulting in $\Delta x \sim 0.008 - 0.04$ m), which provides sufficient grid points to capture the wave shape. Finally, the time step was set at 300 points per wave period (resulting in $\Delta t \sim 0.003 - 0.02$ s) to minimise the numerical dissipation of the waves as they propagated through the relatively large domain.

3.1. Results

Fig. 6 shows the comparison between the model and the analytic solution for this test case. For increasing wave periods, wave reflections reduce as the transmission increases (Fig. 6a-b). The model captures this trend, and the magnitude of the coefficients for the considered range of wave periods (Fig. 6a-c). Similarly, the predicted amplitudes of the two force components agree well with the analytic solution. Furthermore, the model captures the phase difference between F_x and F_z (illustrated by the red line and markers in Fig. 6e).
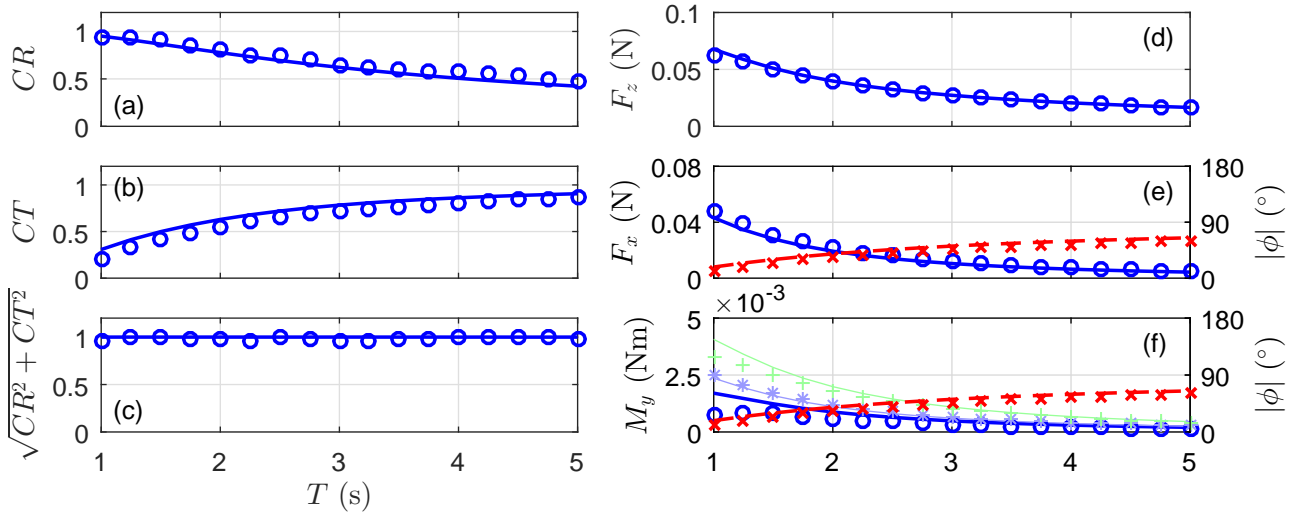

Figure 6: Comparison between the predicted (markers) and analytic results (lines) for the scattering of linear waves by a fixed pontoon. The left panels show the results for the reflection CR (a), transmission CT (b), and combined reflection and transmission coefficients $\sqrt{CR^2 + CT^2}$ (c). The right panels show the results for the amplitudes of the heave force F_z (d), surge force F_x (e), and pitch moment M_y (f). The full line and the circles indicate the amplitude of the hydrodynamic loads. The dashed lines and the crosses in panel (e) and (f) depict the absolute phase difference ($|\phi|$) between the respective load component (F_x or M_y) and F_z. In panel (f), the individual contributions of F_z and F_x to M_y are depicted by the light green and light blue results, respectively.

Compared to the force components, discrepancies are larger for M_y (which is typically under predicted), although its trend and especially its phase difference with F_z are reproduced well (Fig. 6f). The moment is a linear combination of the moment contributions by F_z and F_x. These two contributions are nearly out of

17

phase with each other, and the amplitude of M_y is therefore approximately given by the difference between the amplitude of F_z and F_x. Compared to the amplitude of M_y, the predicted amplitudes of these two contributions agree better with the analytic solution (illustrated by the light blue and light green results in Fig. 6f), although the F_z contribution is under predicted for shorter wave periods. This illustrates that M_z is sensitive to relatively small discrepancies in the force components.

The results of this test case show that the model predictions are in general agreement with the analytic solution for the transmission and reflection coefficients, and the hydrodynamic loads. This demonstrates that two layers are sufficient to capture the scattering of the waves by the pontoon, and the overall magnitude of the hydrodynamic loads that act on the pontoon.

To gain insight in the temporal accuracy of the model when solving a combination of free surface and pressurised flows, a numerical convergence test was conducted for one wave condition of this analytic test case (i.e., the wave with a period of 1 s). For this condition, we conducted a series of simulations with a gradually decreasing time step (starting at 80 points per wave period), for which the numerical solution is expected to converge to a final solution. By taking the root-mean-square-error between the results of the finest and a coarser temporal resolution, we can gain insight in the convergence behaviour and the temporal accuracy of the model. The results of this convergence test confirm that the overall temporal accuracy of the model is first order when predicting the hydrodynamic loads on a floating body (Fig. 7).
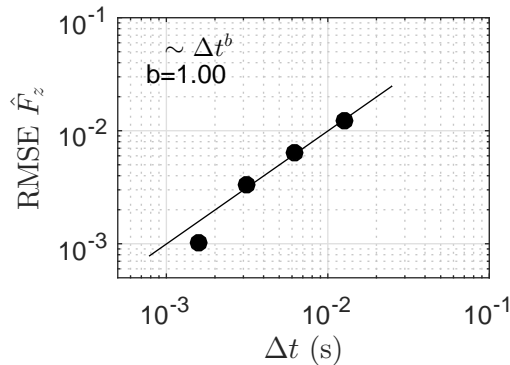

Figure 7: Root-mean-square-error of the heave force amplitude $\hat{F}_z$ for a varying temporal resolution. The markers indicate the computed error, and the line indicates the best fit for the Δt^b power function (in which b is a real number). In the top left corner, the b coefficient of the power function is listed.

4. Scattering of solitary wave by a pontoon

In a similar 2DV set-up as §3, Lin (2006) considered the interactions between a fixed pontoon and a solitary wave. In this test, the still water depth was 1 m, and the pontoon had a width of 5 m and a draft of 0.4 m. The domain had a total length of 100 m, and the centre of the pontoon was positioned at $x = 32.5$ m

18

(see Fig. 8a). In this set-up, Lin (2006) solved the scattering of a solitary wave with a height of 0.1 m using a non-hydrostatic σ−coordinate model and a volume of fluid model. Both models yielded similar results with the same horizontal resolution, but with different vertical resolutions (i.e., 20 layers in the σ−model, and 130 meshes in the VOF model). In this work, we compare our model results with the results of Lin (2006), to demonstrate the capabilities of the present approach. To allow for a fair comparison, the spatial resolution was set in accordance with the study of Lin (2006), except for the vertical resolution. In this work, only 2 layers were employed to discretise the vertical domain. The horizontal grid resolution was set at $\Delta x = 0.05$ m, and the time step at $\Delta t = 0.01$ s.

4.1. Results

After generation at the wavemaker, the solitary wave propagated towards the pontoon, where it partially reflected and transmitted. After interacting with the pontoon, the reflected part of the wave propagated back towards the wavemaker, where it was absorbed. This wave arrived after about 20 s at sensor 1, which is characterised by an initially positive elevation that is followed by a depression and some small oscillations (Fig. 8b). At roughly the same time, the transmitted wave arrived at sensor 2 (Fig. 8c). At both wave sensors, the results of the 2 layer SWASH model and the 20 layer σ-model are in excellent agreement. Naturally, the coarse vertical resolution that was used in this work implies that the model did not capture the vertical structure of the flow field in the vicinity of the structure. Nonetheless, the model captured the partial reflection and transmission of the solitary wave, which demonstrates that the present approach can efficiently resolve its interactions with the pontoon.
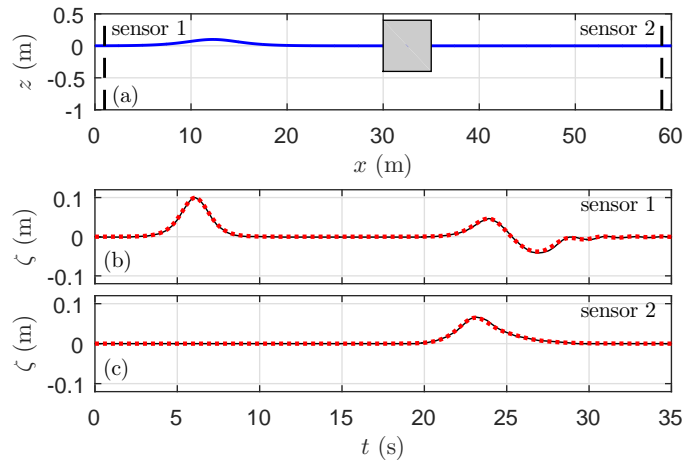

Figure 8: Set-up of the solitary wave test case and snapshot of the free surface at $t = 10$ s (a), and the time series of the free-surface elevation at the two wave sensors (b and c). The black line indicates the solution of the 20 layer model of Lin (2006), and the dotted red line indicates the solution of the 2 layer SWASH model.

19

5. Scattering of regular waves by a pontoon

The third test case considers the scattering of regular waves by a rectangular pontoon that was located inside a wave basin (Wang et al., 2011), see Fig. 9 for an overview of the laboratory set-up. The basin had a constant depth of 0.3 m, except for a deep water region near the wavemaker. The pontoon was restrained by four tripods; and had a width of 0.6 m, a length of 2 m, and a draft of 0.24 m. A total of 14 wave sensors were positioned in the vicinity of the pontoon to measure the surface elevation. A wave absorber was positioned along the right boundary of the wave basin, to minimise wave reflections. In this experiment, a total of six wave conditions were forced at the wavemaker, which varied in wave period ($T = 1.5, 2$, and 3 s) and wave height ($H = 3$, and 6 cm). Here, we consider the steepest wave condition and the weakest nonlinear wave condition of this experiment (i.e., a wave with $H = 6$ cm and $T = 1.5$ s, and a wave with $H = 3$ cm and $T = 3$ s, respectively).
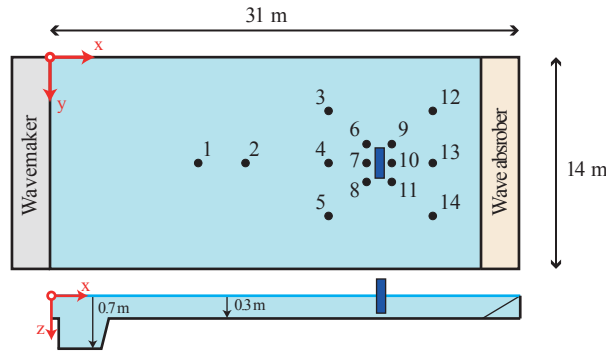

Figure 9: Overview of the experimental set-up. The numbered blue markers indicate the location of the wave sensors, and the blue rectangle indicates the position of the pontoon.

The spatial and temporal resolution of the SWASH model were chosen based on the wave characteristics. The grid resolution was set at $\Delta x = \Delta y = 0.05$ m, corresponding to at least 50 points per wave length. The temporal resolution was set at 100 points per wave period, which resulted in $\Delta t = 0.015 - 0.03$ s. Two vertical layers were used, which is sufficient to capture the wave dispersion for the range of normalised water depths encountered in the deep water region (which varied between $0.6 - 1.4$). A sponge layer of 5 m width was positioned along the right boundary of the basin to dissipate incoming waves.

5.1. Results

Fig. 10 shows the time series of the measured and predicted (normalised) surface elevation for the two wave conditions of this test case. They depict the surface elevation for 6 wave periods, after the initial waves have reached sensors 12-14. In this test case, waves are reflected and transmitted by the pontoon, and wave diffraction occurs in the lee of this body. For the steepest wave case, the first waves reached sensors 12-14
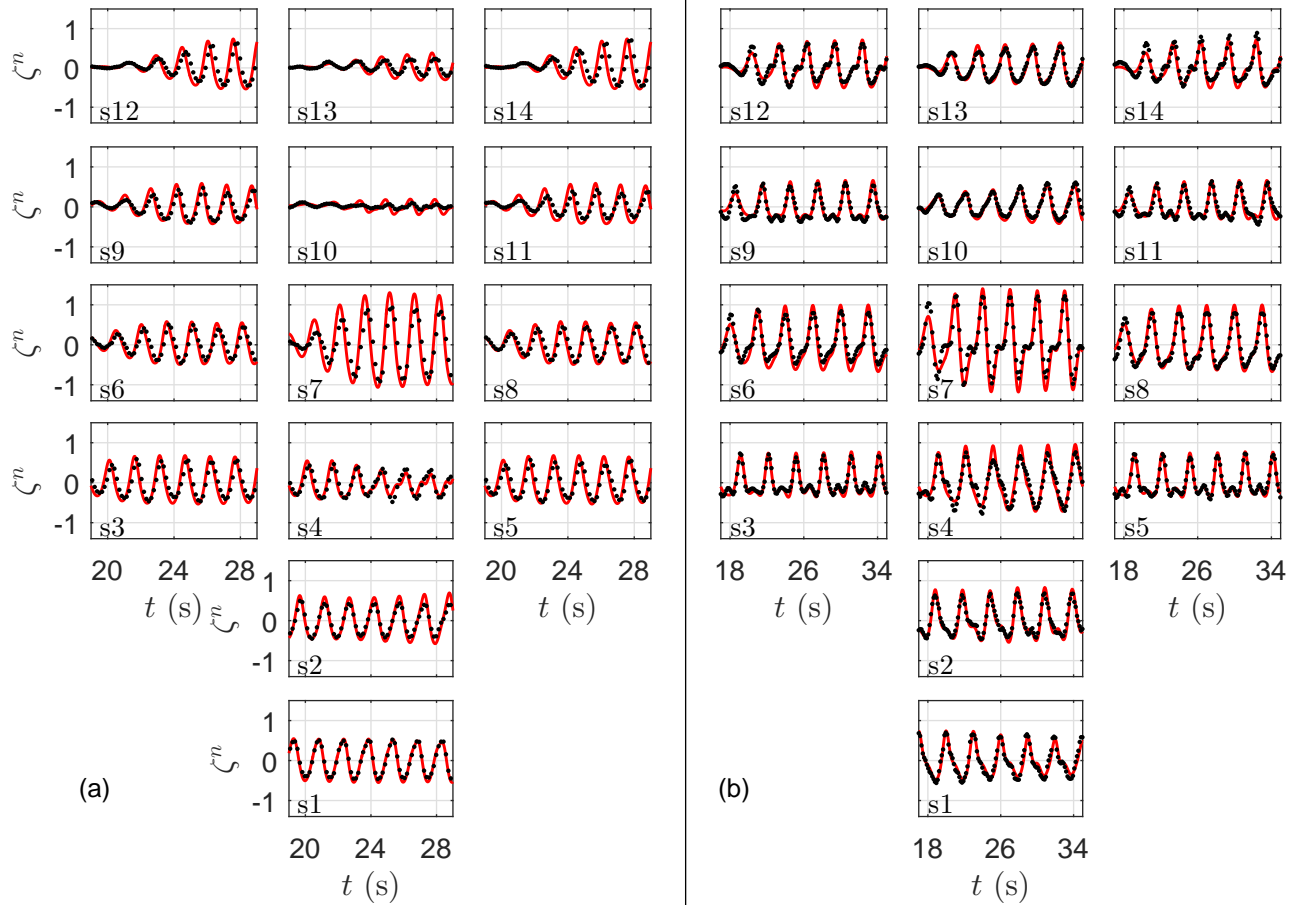
20

Figure 10: Time series of the surface elevation normalised by the incident wave height (ζ^n) at the 14 wave sensors for the steepest wave condition (a), with $H = 6$ cm and $T = 1.5$ s, and for the weakest nonlinear wave condition (b), with $H = 3$ cm and $T = 3$ s. The black dots indicate the measurements, and the red and blue line indicates the model predictions for the steep and weakly nonlinear condition, respectively. In each subplot, the number indicates the position of the respective wave sensor. Please note that the subplots are arranged according to the position of the respective wave sensor in the wave basin.

after approximately 20 s (Fig. 10a). For this relatively short-wave period, the waves reflected significantly at the pontoon and the wave transmission was very small, which is illustrated by the high wave elevation at sensor 7 and the low elevation at sensor 10. Due to the diffraction of waves in the lee of the pontoon, the wave elevation at sensor 13 is larger compared to the signal at sensor 10. At all sensors, the predicted wave signals agree well with the measurements. A small phase difference between the measurements and the predictions can be observed at sensors 12-14 (where the wave field is progressive). This is attributed to a small difference between the analytical and numerical wave celerity ($\sim 0.5\%$). For the simulation that considers a longer wave period, the waves experienced a stronger transmission and diffraction (Fig. 10b). The model reproduced the (irregular) wave elevation that was measured at all sensors, which illustrates that it captured this pattern. Overall, the model predictions agree well with the measurements of this laboratory

21

experiment. These results demonstrate that the model captures the scattering of regular waves, and the diffraction in the lee of a rectangular pontoon.

6. Wave impact on a container ship

The last test case considers the wave impact on a restrained container ship for a range of wave conditions (Bijleveld, 2004; Van der Molen, 2006). This experimental campaign was conducted in a wave basin that measured approximately 40×40 m^2. In the campaign, a restrained ship, located either in open water or in a harbour basin, was subject to a range of wave conditions, including realistic short-crested sea states (see Fig. 11 for a sketch of the experimental set-up). The still water depth in the basin was 0.2 m. To prevent reflections at the side walls of the basin, gravel beaches were constructed along parts of the basin boundaries. When the harbour basin was present, a gravel slope was positioned at the harbour wall that faced the wavemaker to reduce reflections.
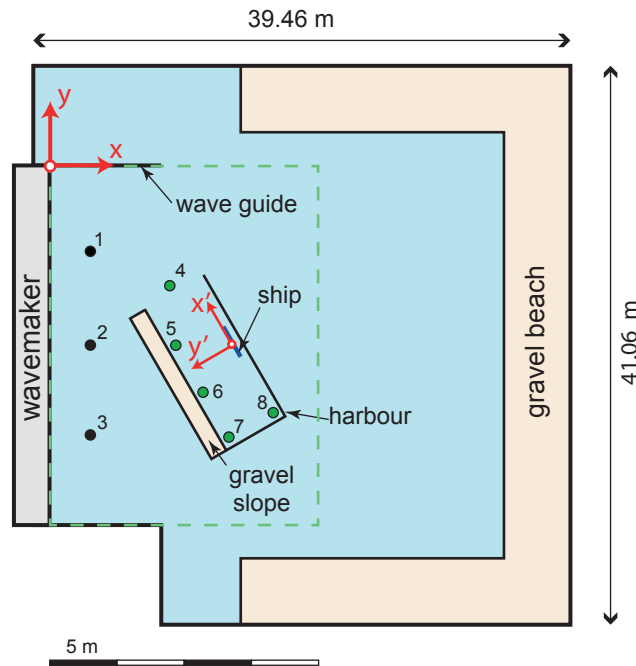

Figure 11: Overview of the laboratory set-up, including the harbour and the location of the ship. The numbered circles indicate the location of the wave sensors. Sensors 1-3 were present during all experiments, and sensors 4-8 were only available for the experiments which included the harbour basin. The thin dashed green line illustrates the region of interest.

The ship, a 1 : 100 scale model of a Panamax container ship, was restrained by six force transducers that fixed the ship to a steel frame. Based on these transducers, the forces and moments were measured relative to a ship coordinate system ($x' - y'$, illustrated in Fig. 11), in which the horizontal coordinates are rotated with 120° relative to the global coordinate system ($x - y$ in Fig. 11). With this set-up, small

22

Table 1: Wave parameters at the wavemaker for the irregular wave conditions of the experimental program. Listed are the wave height H_{m0}, the peak wave period T_p, the directional distribution of the wave spectrum $D(\theta)$ (which was constant over the frequencies), and the duration of the experiment $T_{\exp}$. The directional distribution is defined as $D(\theta; f) = \frac{S_\zeta(f, \theta)}{S_\zeta(f)}$ (e.g., Holthuijsen, 2007), where $S_\zeta(f, \theta)$ is the frequency-direction spectrum and $S_\zeta(f)$ is the frequency spectrum of the surface elevation (see also Appendix B.1). $D(\theta) = \delta$ corresponds to long-crested waves, in which δ is the Dirac delta function. The mean wave angle of all wave conditions is perpendicular to the wavemaker.

	$H_{\mathrm{m}0}$ (cm)	T_p (s)	$D(\theta)$	T_{exp} (min)
OWi1	1.5	1.0	δ	30
OWi2	1.5	1.5	δ	30
OWi3	1.5	1.0	$\cos^2(\theta)$	30
OWi4	1.5	1.5	$\cos^4(\theta)$	30
HBi1	3.0	1.0	δ	45
HBi2	3.0	1.5	δ	45
HBi3	3.0	1.0	$\cos^2(\theta)$	45
HBi4	3.0	1.5	$\cos^2(\theta)$	45

534 measurement errors in the forces can induce significant errors in the moments, and the roll moment in
535 particular (e.g., Van der Molen, 2006). Nonetheless, we compare the model results and the measurements
536 for all load components, but we anticipate that discrepancies are typically larger for the moments than for
537 the forces. Several wave sensors were positioned inside the basin to measure the surface elevation. Near the
538 wavemaker, three sensors were present for all simulations. For the simulations in which the harbour basin
539 was present, five additional wave sensors were positioned in the vicinity of the ship (see Fig. 11).

540 Waves were forced using a piston-type wavemaker, including second-order wave control and reflection
541 compensation. The wave conditions varied from monochromatic to short-crested waves. In this paper, we
542 distinguish between the conditions in which the ship was moored in open water (labelled as OW) or inside
543 the harbour basin (labelled HB). We consider a total of ten wave conditions: two regular wave conditions
544 (labelled as OWr and HBr) and eight irregular wave conditions (with the label OWi and HBi). In the regular
545 wave experiments, which had a duration of 10 min, a monochromatic wave was forced with an amplitude
546 of 1 cm, a period of 1 s, and a direction perpendicular to the wavemaker. In the irregular experiments,
547 both long-crested and short-crested wave fields were generated, of which the bulk wave parameters are listed
548 in Table 1. In these test cases, the wave conditions differed mainly in the wave period, and in directional
549 spreading. They varied from long-crested waves with a relatively long peak period (e.g., OWi2 and HBi2),
550 to short-crested sea states with relatively short peak periods (e.g., OWi3 and HBi3).

551 Similar to the previous test cases, the temporal and spatial grid resolution of the model were chosen based
552 on the characteristics of the wave conditions. Two vertical layers were sufficient to capture the dispersion of
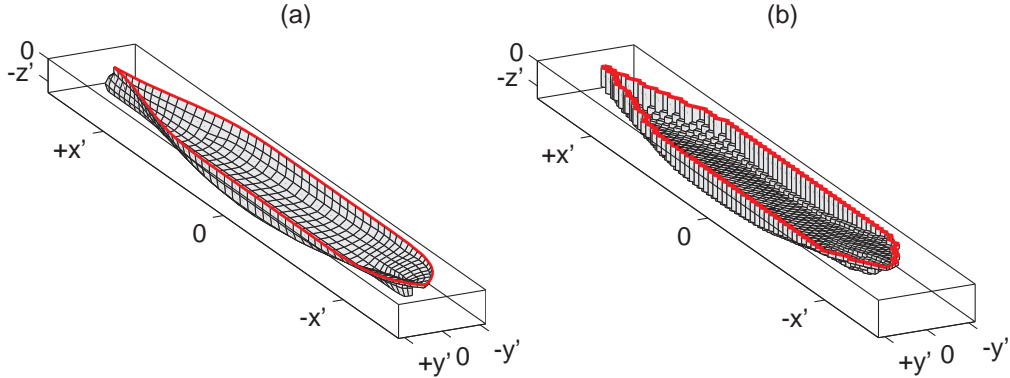
Figure 12: Sketch of the ship hull in the ship coordinate system. (a) Panel model of the Panamax ship. (b) Single valued ship function $S(x', y')$ used in the SWASH computations. The thick red line in (a) and (b) indicates the waterline contour.

the dominant waves (for which the kd values ranged $0.6 - 3.2$). The grid resolution was set at $\Delta x = 0.02$ m and $\Delta y = 0.035$ m, which corresponds to at least 20 points per wave length for frequencies up to $2f_p$, where $f_p (= 1/T_p)$ is the peak frequency. The time step was set at 0.01 s, which corresponds to at least 50 points per wave period for frequencies up to $2f_p$. To reduce the computational effort, we reduced the domain size in both horizontal directions. The resulting numerical domain spans approximately 30×36 m^2. Furthermore, the grid resolution was set to increase linearly away from the region of interest (illustrated by the dashed green line in Fig. 11), with a maximum grid resolution of 0.25m. The Manning roughness coefficient was set at the default value used in SWASH, $n = 0.019$ s/m$^{1/3}$. Waves were generated at the numerical wavemaker using weakly nonlinear wave theory to include the bound infragravity waves (Rijnsdorp et al., 2015), based on the wave parameters of the laboratory experiment (e.g., Table 1). The model simulations were run with the same duration as the laboratory experiment, except for the regular wave conditions which were run for 5 min (corresponding to $\sim$300 waves). The wave guides, harbour walls, and gravel slopes were schematised as a porous structure (see Appendix A for a brief description). The impermeable wave guides and harbour walls were schematised with a porosity equal to zero, and the gravel slopes were schematised with a porosity of 0.45, and a characteristic stone size of 2 cm.

In the numerical model, the hull of the ship is represented as a single valued function in $x - y$ space. A panel model of the Panamax ship (Fig. 12a) was converted into a single valued function (Fig. 12b) by interpolating the panel elements that were located within the waterline contour to the computational grid used in SWASH. Because the ship is represented as a single valued function in $x - y$ space, the bulbous bow of the ship is not included in this schematisation. This model limitation will likely affect the predictions of the hydrodynamic loads that act on the body, as the bulbous bow alters the flow field in the vicinity of the ship (e.g., Bertram, 2012).

Animations of the simulated wave field for OWi1 and HBi4 are included in the supplementary material.
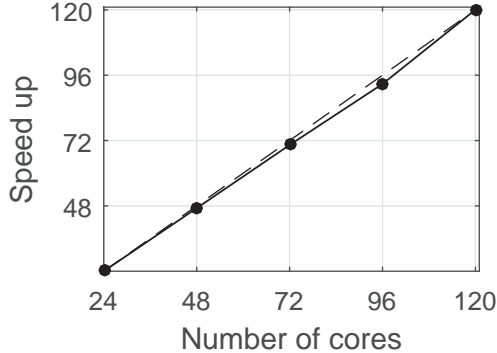
24

Figure 13: Scaling of the Cartesius supercomputer (40960 Intel Xeon cores, $2.4 - 2.6$GHz with 64GB internal memory). The line with the markers represents the model speed up. The dashed line illustrates a linear speed up (i.e., if the number of cores is doubled the computational time is halved).

Although the set-up of this experiment is relatively simple, it provides a demanding test case for the numerical model as it includes many features that are representative for a real harbour. For example, it includes the reflection and diffraction of waves by the presence of quay walls, and a realistic ship model. Furthermore, the size of the domain and the duration of the simulation are representative for a realistic harbour or coastal region. At prototype scale, this experimental set-up corresponds to a domain that spans approximately 4×4 km ($20 - 30$ dominant wave lengths), and a duration of $5 - 7.5$ hr ($1200 - 2700$ dominant wave periods). Given these scales, all simulations of this laboratory experiment were ran with 120 cores on Cartesius, the Dutch national supercomputer. The model showed an excellent parallel scaling on Cartesius (Fig. 13). The regular wave simulations took on average 4 hr to run, and the irregular wave simulations took on average 32 hr to run. This makes the computational effort significant, but viable on present day multi-processor machines.

6.1. Results

The model results and measurements are compared based on time series for the regular wave conditions, and based on spectral results for the irregular wave conditions. We compared spectral results for the irregular wave conditions instead of time series as they allow us to gain more insight in the frequency dependence of the wave field and the hydrodynamic loads. In the following, we will focus on the results of the irregular sea states. The results of the two regular wave conditions can be found in Appendix C.

To assess the model performance quantitatively, several bulk parameters were computed: the root-mean-square wave height (H_{rms}) and the mean wave period (T_{m02}) for the wave field, and the bulk load (e.g., $F_{x',\mathrm{rms}}$) and mean load period (e.g., $F_{x',\mathrm{m02}}$) for the hydrodynamic loads (see Appendix B.1). Based on these bulk parameters, two statistical measures were computed to quantify the model performance: the relative bias RB and the scatter index SI (see Appendix B.2). In this work, we qualify the model-data agreement

25

as follows: measures < 15% are considered good, measures between 15% and 30% indicate reasonable agreement, and measures > 30% indicate significant discrepancies.

First, we discuss detailed spectral results of the surface elevation and hydrodynamic loads for two rep-
resentative simulations. These two simulations represent the results with the best and the worst overall
scatter index (SI). This overall SI was computed by averaging the SI over all bulk parameters. The first
simulation (case OWi4) corresponds to the lowest SI value (best comparison), and the second (case HBi3)
corresponds to the highest SI value (worst comparison).

For the simulation with the lowest scatter index (OWi4), the ship was moored in open water and subject
to a short-crested wave field (Table 1). The model reproduced the typical shape and the energy levels of
the surface elevation spectra S_ζ near the wavemaker (Fig. 14a), except for an over prediction near f_p. This
is confirmed by the bulk wave parameters (|RB| < 0.08). The predicted and observed wave spectra are
comparable to the target wave spectrum (depicted by the dash-dot gray line in Fig. 14a). This indicates
that the wave field was dominated by the waves generated at the wavemaker, and that the influence of waves
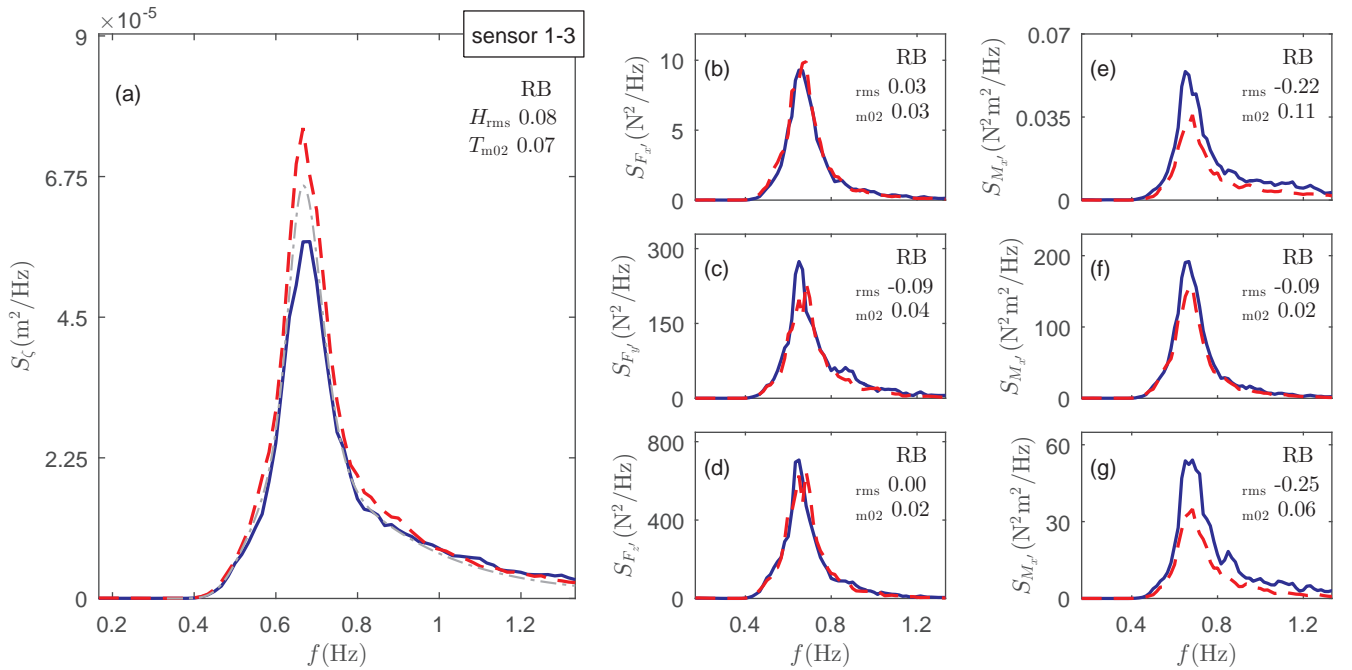reflected at the ship was relatively small. Therefore, these results illustrate that the wavemaker in the model

Figure 14: Predicted (red line) and observed (blue line) spectra of the surface elevation S_ζ (a), and the forces S_F (b-d) and moments S_M acting on the ship (e-g) for OWi4. The surface elevation spectra plotted in panel (a) is the average of the spectra at sensor 1-3. In panel (a), the thin dash-dot gray line indicates the target JONSWAP spectrum with which the physical and numerical wavemakers were forced. In each panel, the relative bias (RB) of the two bulk parameters are depicted in the top right corner. For brevity, the bulk loads are denoted with $_{rms}$, and the mean load periods are denoted with $_{m02}$.

reproduced the wave field that was generated in the laboratory experiment.

The spectral shape of the observed force and moment spectra is similar to S_ζ (Fig. 14b-g versus Fig. 14a). The predicted force and moment spectra generally agree well with the measurements, especially for the three force components and the pitch moment ($M_{y'}$). This is confirmed by the low RB values of their bulk parameters ($|\text{RB}| < 0.09$), which indicate that they were reproduced with a similar accuracy as that of the wave field. In contrast, the predicted $M_{x'}$ and $M_{z'}$ show bigger discrepancies as their spectral levels are under predicted. Nonetheless, their spectral shape was reproduced well and their bulk parameters were predicted with reasonable accuracy ($|\text{RB}| < 0.25$).

In HBi3, the ship was moored inside the harbour and subject to a short-crested wave field (Table 1). The predicted spectra and bulk wave parameters agree with the measurements near the wavemaker (Fig. 15a). Here, the wave field is dominated by the waves generated at the wavemaker as the spectra compare well with the target wave spectrum. In the harbour basin, the predicted and observed wave spectra and bulk wave parameters are in good agreement ($RB \leq 0.11$), although discrepancies were generally larger compared to
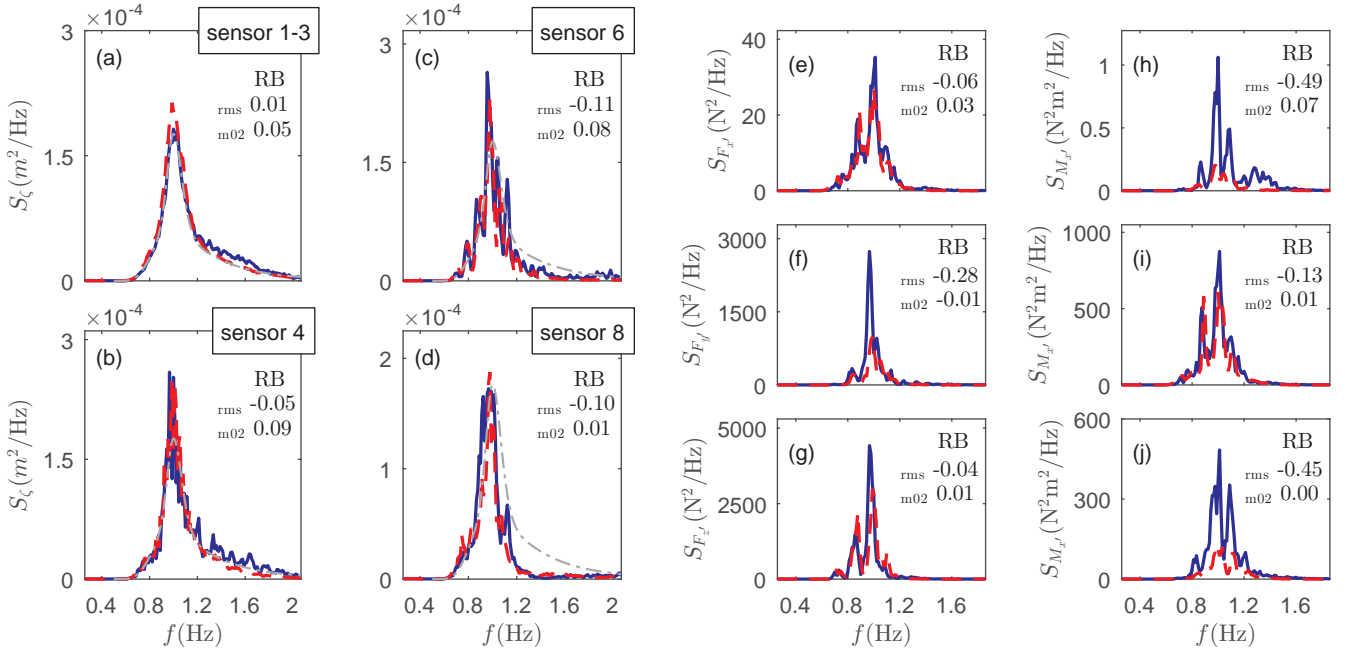

Figure 15: Predicted (red line) and observed (blue line) spectra of the surface elevation S_ζ (a-d), and the forces S_F (e-g) and moments S_M acting on the ship (h-j) for HBi3. The plotted surface elevation spectra in panel (a) is the average of the spectra at sensor 1-3. The surface elevation spectra in panel (b-d) are the results at sensors 4, 6, and 8, respectively (see Fig. 11 for the sensor positions). In panel (a-d), the thin dash-dot gray line indicates the target JONSWAP spectrum with which the physical and numerical wavemakers were forced. In each panel, the relative bias (RB) of the two bulk parameters are depicted in the top right corner. For brevity, the bulk wave heights and loads are denoted with $_\text{rms}$, and the mean wave and load periods are denoted with $_\text{m02}$.

27

the results at the sensors near the wavemaker. Furthermore, the model captured the irregularity of the wave spectra, which is indicative for the occurrence of a (partially) standing wave field. These results show that the model captures the overall wave field in the harbour.

Overall, the spectral shape and the spectral levels were reproduced well for the three force components (Fig. 15e-g), including most of the distinct spectral features (e.g., the additional peaks in F_z', see Fig. 15g). The forces on the moored ship were reproduced with larger discrepancies compared to the wave field, although the errors in the bulk parameters were of similar order ($|RB| \leq 0.28$ versus $RB \leq 0.11$). In contrast with the forces, the moments were predicted with significant errors (Fig. 15h-j). Only M_y' was reproduced well (Fig. 15i), both in terms of the irregular spectral shape and the bulk moment parameters (for which $|RB| \leq 0.13$).

To present the main findings of this test case, Fig. 16 and Table 2 show a comparison between the predicted and measured bulk parameters for all conditions that were considered. Near the wavemaker, the predicted H_{rms} agree well with the measurements (blue dots in Fig. 16a). Inside the harbour basin, the
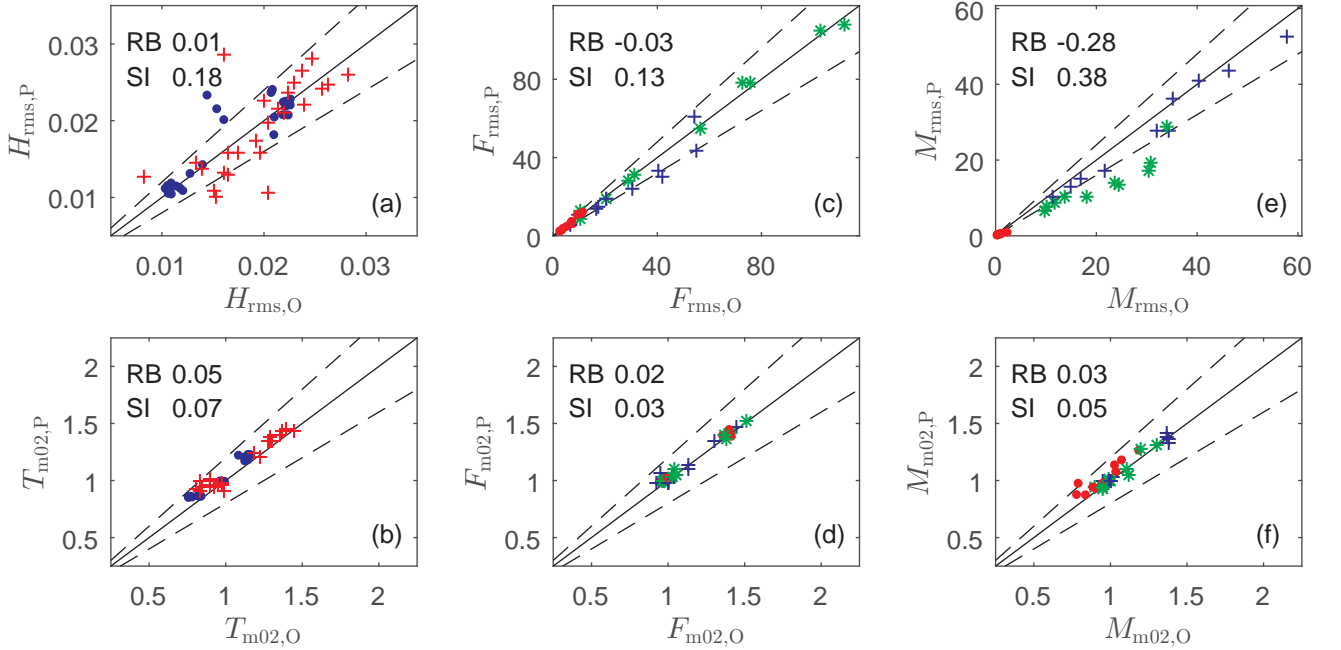

Figure 16: Predicted (subscript P) versus observed (subscript O) wave height H_{rms} (a), mean wave period T_{m02} (b), bulk force F_{rms} (c), mean force period F_{m02} (d), bulk moment M_{rms} (e), and mean moment period M_{m02} (f). The solid black line indicates perfect agreement, and the dashed black lines indicate the 20% error bands. In each panel, the overal relative bias (RB) and scatter index (SI) are printed in the top left side. In panel (a) and (b), results of a sensor located outside the harbour are indicated by a blue dot, and results of a sensor located inside the harbour are indicated by a red plus. In panel (c-f), the color and type of the marker indicates the direction of the parameter. That is, a red dot indicates the x' component, a blue plus the y' component, and a green asterisk the z' component.

scatter is typically larger (red pluses in Fig. 16a). Overall, the model reproduced the wave height with a scatter of 18%. Note that the average RB is smaller than SI, because H_{rms} is both over and under predicted. The outliers in Fig. 16a correspond to case HBr (see Fig. C.2). The model systematically over predicted T_{m02} with a relatively small bias of 5% (Fig. 16b), and there is no clear difference between predictions outside or inside the harbour. Overall, the discrepancies between the predictions and measurements are larger in subset HB than in OW (Table 2). This is likely related to the increased complexity of the conditions in subset HB, as a standing wave pattern occurred inside the harbour basin.

The bulk forces and the mean force periods were predicted with an accuracy that is comparable to the wave field (Fig. 16c-d). The F_z' and F_y' force components were typically an order of magnitude larger than F_x', whereas their mean periods were similar. These trends were reproduced well by the model. Overall, F_z' was reproduced with good statistical agreement ($SI \leq 0.05$, see Table 2). Discrepancies were larger for the horizontal force components F_x' and F_y', which were in reasonable agreement with the measurements ($SI \leq$ 0.12 and $SI \leq 0.22$, respectively, see Table 2). In contrast to the forces, the bulk moments were predicted with significant deviations (Fig. 16e), although their mean periods agreed well (Fig. 16f). Discrepancies

Table 2: Statistical measures (relative bias RB, and scatter index SI) of the wave parameters (significant wave height and mean wave period), and the hydrodynamic loads (forces and moments) for the simulations with a ship moored in open water (OW), a ship moored inside a harbour basin (HB), and for all simulations combined (Overall).

	OW		HB		Overall	
	RB	SI	RB	SI	RB	SI
H_{rms}	0.02	0.12	0.01	0.19	0.01	0.18
$T_{\mathrm{m_{02}}}$	0.06	0.07	0.05	0.07	0.05	0.07
$F_{x',\mathrm{rms}}$	-0.09	0.14	0.07	0.10	0.02	0.12
$F_{y',\mathrm{rms}}$	-0.10	0.14	-0.13	0.20	-0.12	0.22
$F_{z',\mathrm{rms}}$	-0.01	0.07	0.01	0.04	0.00	0.05
$M_{x',\mathrm{rms}}$	0.22	0.24	-0.48	0.59	-0.42	0.63
$M_{y',\mathrm{rms}}$	-0.16	0.19	-0.05	0.08	-0.09	0.11
$M_{z',\mathrm{rms}}$	-0.34	0.44	-0.34	0.36	-0.34	0.39
$F_{x',\mathrm{m_{02}}}$	0.02	0.02	0.01	0.02	0.01	0.02
$F_{y',\mathrm{m_{02}}}$	0.04	0.05	-0.01	0.02	0.02	0.04
$F_{z',\mathrm{m_{02}}}$	0.03	0.03	0.01	0.01	0.02	0.02
$M_{x',\mathrm{m_{02}}}$	0.11	0.12	0.06	0.06	0.08	0.10
$M_{y',\mathrm{m_{02}}}$	0.01	0.02	0.00	0.03	0.01	0.02
$M_{z',\mathrm{m_{02}}}$	0.03	0.04	-0.02	0.04	0.00	0.04

were typically largest for the M'_x and M'_z moment ($SI \le 0.63$ and $SI \le 0.39$, respectively), whereas M'_y was reproduced with an SI that is comparable to the forces (see Table 2). These findings mirror the results of the individual force components. For example, the error in M'_x (which depends on F'_y and F'_z) is larger than the error in M'_y (which depends on F'_x and F'_z) as the error in F'_y is larger than the error in F'_x (see Table 2). These results highlight the sensitivity of the moments to relatively small discrepancies in the force predictions. Although the errors in the predicted moments were significant, the model captured the variation of the bulk moments for the variety of wave conditions that were considered in this work (Fig. 16e).

To summarise, these findings show that the wave-induced forces were predicted with an accuracy that is comparable to the wave field, whereas the moments were predicted with more significant discrepancies. This is not surprising given the relatively coarse schematisation of the ship's hull (e.g., the bulbous bow was not included in the simulations), and to difficulties in measuring the moments that act on a restrained ship (e.g., Van der Molen, 2006). Overall, the results of this test case demonstrate the potential of the model in seamlessly simulating the wave field in the basin, their interactions with the restrained ship, and the resulting hydrodynamic loads that act on the body.

7. Discussion

This paper presents a new numerical approach to simulate the nonlinear evolution of waves and their impact on a restrained ship at the scale of a realistic harbour or coastal region. This model is based on the non-hydrostatic approach, and the SWASH model in particular, which is in essence a direct numerical implementation of the RANS equations. The use of the Keller-Box scheme to discretise the non-hydrostatic pressure allows such models to efficiently resolve a range of nearshore wave and flow phenomena. To include the interactions between the waves and the ship, we developed a new method to account for the presence of a floating body in the non-hydrostatic approach. The findings of this work demonstrated that the model captures the scattering of regular waves and a solitary wave by a rectangular pontoon. Furthermore, the model gave a reasonable prediction of the magnitude and periodicity of the hydrodynamic loads on a restrained container ship for a range of realistic wave conditions. Most importantly, this work demonstrated that a coarse vertical resolution sufficed to capture these interactions, which highlights that the model retains this favourable property of the non-hydrostatic approach when a floating body is included.

Compared to the variety of models that have been developed to solve the wave-ship interactions (e.g., Newman, 2005; Hadžić et al., 2005; Yan and Ma, 2007; Bouscasse et al., 2013), the primary advantage of the present approach is that it does not rely on predictions of the wave field in the vicinity of the moored ship. To date, the most advanced methodology that was developed to solve both the evolution of waves and their impact on a moored ship coupled a wave model based on the Boussinesq or non-hydrostatic approach with

30

a panel model (Bingham, 2000; Van der Molen and Wenneker, 2008; Dobrochinski, 2014). This coupled approach includes a detailed schematisation of the ship's hull, but is restricted to relatively mild wave conditions, whereas the present approach makes no a-priori assumptions concerning the nonlinearity of the wave field, but is limited to a relatively coarse ship schematisation. Although a direct comparison between these two methods was not the subject of this work, we can make an indirect comparison based on the work of Dobrochinski (2014). In this study, a coupled model (combining SWASH and a panel model) was validated for several wave conditions belonging to the same laboratory experiment that was considered in the present work (§6). Overall, the discrepancies in the hydrodynamic load predictions of this coupled model are comparable to the results presented here (§6.1). This suggests that the accuracy of these two methods is similar for these experimental conditions.

The key features of the present approach are thus that (i) it can relatively efficiently resolve the evolution of waves in coastal waters (Zijlema et al., 2011; Smit et al., 2013, 2014), including the infragravity waves which are known to disrupt harbour operations (Rijnsdorp et al., 2014, 2015; De Bakker et al., 2016), and (ii) that it can seamlessly account for the interactions between the waves and a restrained ship. This demonstrates that the model provides a promising new alternative to simulate the nonlinear evolution of waves and their impact on a restrained ship at the scale of a harbour or coastal region. Based on these considerations, we believe that this work provides a crucial first step towards the development of a new approach to simulate the wave-induced response of a ship that is moored in coastal waters.

So far, the model was used to simulate the wave impact on a restrained ship under idealised conditions (e.g., relatively mild waves, and a relatively simple harbour layout). Further research is therefore required to push the capabilities of the approach towards more realistic conditions. This includes an assessment of the model capabilities for more challenging environments, for example, in a complex coastal region or in the case of significant nonlinear wave effects. Furthermore, future work can be undertaken to resolve the actual wave-induced motions of a moored ship, and to improve the accuracy of the model in resolving the wave-ship interactions. In this study, the model was applied with a relatively coarse vertical resolution, which permits applications at relatively large scale. On the other hand, this implies that the model does not resolve the details of the vertical flow structure in the vicinity of the ship, which are likely important in the case of energetic wave conditions (or significant ship motions) when turbulent effects are significant. Given the flexibility of the non-hydrostatic approach (in contrast to the coupled wave-panel methodology), resolving such features merely requires an increase of the vertical resolution near the ship combined with the use of a proper turbulence model. For example, by implementing a domain decomposition technique, the model can retain its favourable features in simulating nonlinear waves at large scales, while it at the same time can resolve the vertical flow structure in the vicinity of the moored ship.

31

Appendix A. Porous flow

To account for the flow through a porous structure, the governing equations are adapted in accordance with Madsen (1983). In SWASH, only the global continuity and the horizontal momentum equation are adapted to include the effect of the flow through a porous structure, whereas the vertical momentum equation is not adapted. Although an inclusion of the porous influence in the vertical momentum equation is likely more accurate (e.g., Higuera et al., 2014; Ma et al., 2014a; Jacobsen et al., 2015), we are not primarily interested in the flow through a porous medium. We merely mimic the dissipation induced by a gravel beach, and the reflections induced by impermeable walls, for which this approach is expected to be sufficiently accurate.

The modified equations in the outer domain read,

$$n\frac{\partial \zeta}{\partial t} \quad + \quad \frac{\partial HU}{\partial x} = 0,$$

$$\frac{\partial u_n}{\partial t} \quad + \quad \frac{\partial u_n u_n}{\partial x} + \frac{\partial wu}{\partial z} = -g\frac{\partial \zeta}{\partial x} - \frac{\partial p}{\partial x} + \frac{\partial \tau_{xx}}{\partial x} + \frac{\partial \tau_{xz}}{\partial z} - f_l u - f_t u|u|,$$

where n is the porosity, $u_n \left(= \frac{u}{n}\right)$ is the seepage velocity inside a porous medium, f_l is a laminar friction factor, and f_t is a turbulent friction factor. The friction factors are given by (e.g., Madsen, 1983),

$$f_l \quad = \quad \alpha_e \frac{(1-n)^3}{n^2}\frac{\nu}{D},$$

$$f_t \quad = \quad \beta_e \frac{1-n}{n^3}\frac{1}{D},$$

where ν is the kinematic viscosity of water, D is a characteristic stone size, and α_e and β_e are empirical coefficients. In this study, the empirical coefficient were set at their default values ($\alpha_e = 1000$, and $\beta_e = 2.8$).

Appendix B. Quantitative model-data comparison

Appendix B.1. Bulk parameters

To quantify the model performance for the laboratory experiment of §6, we computed several bulk parameters that represent the wave conditions inside the laboratory basin, and the hydrodynamic loads that

act on the ship. We characterise the wave conditions using the root mean square wave height $H_{\mathrm{rms}} = \sqrt{8\mathrm{m}_0}$ and the mean wave period $T_{\mathrm{m}_{02}} = \sqrt{\mathrm{m}_0/\mathrm{m}_2}$, in which $m_n = \int f^n S_\zeta(f)\mathrm{d}f$, and $S_\zeta(f)$ is the surface elevation spectrum. The H_{rms} provides a measure of the total wave energy, and $T_{\mathrm{m}_{02}}$ provides a measure of the mean wave period. Furthermore, $T_{\mathrm{m}_{02}}$ gives some information on the frequency distribution of the wave energy. Similar to the bulk wave parameters, we computed bulk parameters for the hydrodynamic loads to gain insight in the overall forces and moments acting on the ship. The bulk parameters were computed for each individual component, following the same methodology as the wave height and the mean wave period. For example, the bulk force in x' direction is computed as $F_{x',\mathrm{rms}} = \sqrt{8\mathrm{m}_0}$, in which $m_0 = \int S_{F_{x'}}(f)\mathrm{d}f$, and $S_{F_{x'}}$ is the spectrum of $F_{x'}$. All spectra were computed with 60 degrees of freedom, based on ensemble averaged Fourier-transforms of detrended and windowed signals. To account for the spin-up time of the model and the measurements, the first 80 s of the signals was excluded in the case of a regular wave experiment, and the first 120 s were excluded in the case of an irregular wave experiment (see §6 for a description of the experiments).

Appendix B.2. Statistical measures

We quantified the model performance with two statistical measures: the relative bias, and the scatter index. The relative bias is computed as,

$$\mathrm{RB} = \frac{\sum\limits_{i=1}^{N} \left(Q_p^i - Q_o^i\right)}{\sum\limits_{i=1}^{N} Q_o^i}, \qquad (\text{Appendix B.1})$$

and the scatter index is computed as,

$$\mathrm{SI} = \frac{\sqrt{\frac{1}{N}\sum\limits_{i=1}^{N} \left(Q_p^i - Q_o^i\right)^2}}{\frac{1}{N}\sum\limits_{i=1}^{N} Q_o^i}, \qquad (\text{Appendix B.2})$$

where Q_p is a predicted parameter, and Q_o is an observed parameter in a sample of size N. We computed these statistical measures for the parameters of several groups of simulations. In total we considered three groups, of which one represents all simulations, and of which the two others represent the two simulation subsets (OW and HB). The measures were computed for each bulk parameter of the forces and moments (e.g., $F_{x',\mathrm{rms}}$), by taking the summation over the simulations belonging to a group (i.e., $N = 5$ for group OW and HB, and $N = 10$ for the group that contains all simulations). For the wave heights and mean periods, the measures were computed by taking the summation over all available wave measurements in the group.

Appendix C. Regular wave impact on a container ship

Appendix C.1. Open water

First, we compare predictions and measurements of the surface elevation and hydrodynamic loads for OWr, in which the moored ship was subject to a monochromatic wave. In this experiment, the first waves arrived at the wave sensors after approximately 10 s (Fig. C.1a-c), and about 10 s later they reached the moored ship (Fig. C.1d-i). The signals are roughly sinusoidal for $t > 60$ s, which indicates that the conditions became approximately stationary. Due to the orientation of the ship with respect to the wave direction, the sway force $(F_{y'})$ is slightly larger compared to the surge force $(F_{x'})$. Furthermore, the pitch and yaw moment ($M_{y'}$ and $M_{z'}$, respectively) are an order of magnitude larger compared to the roll moment
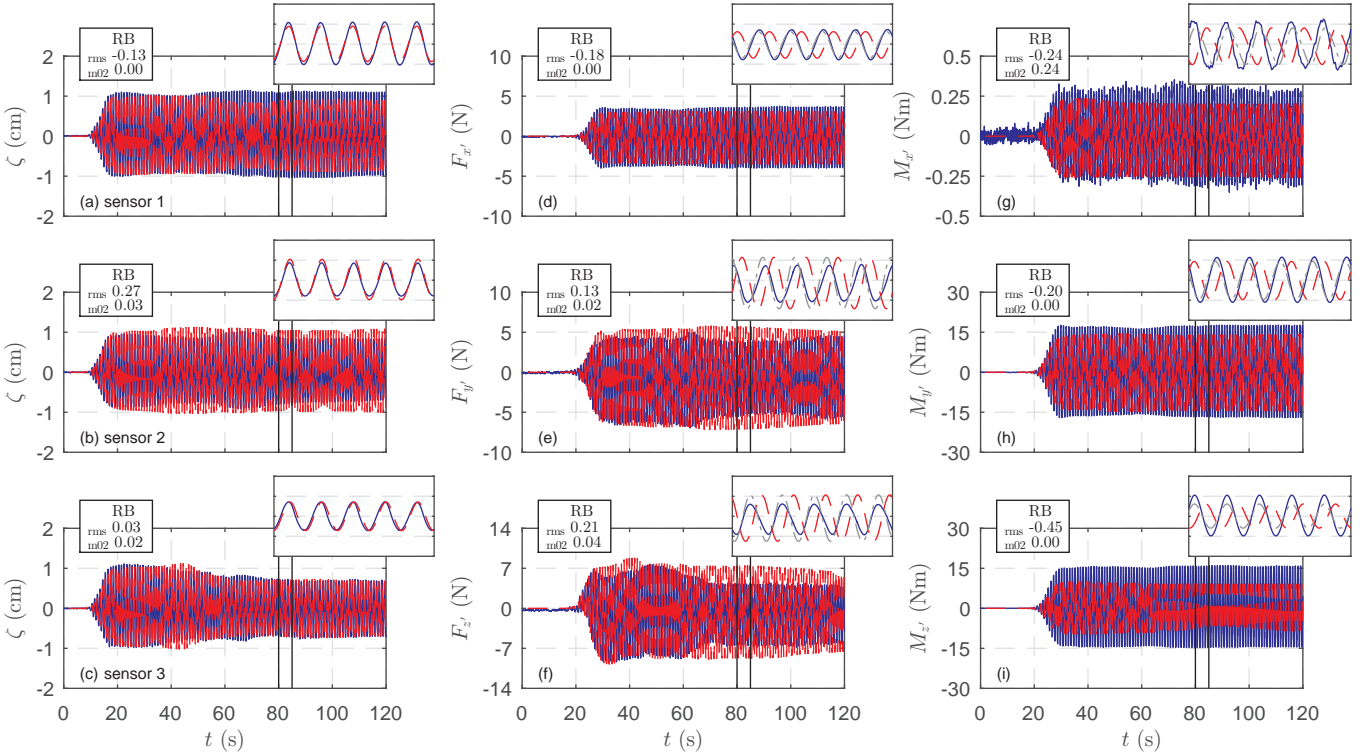

Figure C.1: Predicted (dashed red line) and observed (blue line) time series of the surface elevation ζ (a-c), and the forces F (d-f) and moments M acting on the ship (g-i) for the first two minutes of simulation OWr. The insets adjacent to the main panels show a close up of the results for $80 \leq t \leq 85$ s (illustrated by the two vertical black lines in the main panels). To facilitate a comparison between the predicted and observed hydrodynamic load signals, the dash-dot gray line in the insets of (d-i) shows the predicted hydrodynamic load signal including a time shift of -0.35 s. In each panel, the relative bias (RB) of the two bulk parameters are depicted in the top left corner. In panel (a-c), the RB of the wave height H_{rms} and the mean wave period T_{m02} are shown. In panel (d-i), the RB of the bulk hydrodynamic loads (e.g., $F_{x',\mathrm{rms}}$) and the mean period of the loads (e.g., $F_{x',\mathrm{m02}}$) are shown. For brevity, the bulk loads are denoted with $_{\mathrm{rms}}$, and the mean load periods are denoted with $_{\mathrm{m02}}$. Note that in this case the scatter index is equal to the absolute value of RB.

$(M_{x'})$. Note that the $M_{x'}$ signal is relatively noisy, as its measurements suffer from significant inaccuracies (e.g., Van der Molen, 2006).

The model reproduced the typical surface elevation signal at the wave sensors (Fig C.1a-c), and the predicted wave height and wave period were in reasonable agreement with the measurements ($|\text{RB}| \leq 0.27$). The agreement appears best at the start of the simulation ($t < 30$ s), when the wave field at the sensors was progressive. This illustrates that the model reproduced the monochromatic wave that was generated at the numerical wavemaker. For $t > 30$ s, discrepancies between the predicted and observed surface elevation signals can be observed at all wave sensors. At this time, the waves that were reflected at the ship and at the wave guides reached the wavemaker and were (partly) absorbed. These discrepancies are in part related to errors in the scattering of waves at the ship, and to differences between the absorption characteristics of the physical and numerical wavemaker.

The discrepancies between the predicted and measured load signals are typically larger compared to the surface elevation signals, especially for $M_{z'}$ (which is under predicted with 44%, see Fig. C.1i). Furthermore, the predicted signals are shifted in time with respect to the measurements. Applying the same time shift of -0.35 s to all load signals (illustrated by the dash-dot gray line in the insets of Fig. C.1d-i), the phases of the predicted loads are comparable to the measurements. This shows that the predicted hydrodynamic loads experience the same phase shift, indicating that the relative phasing of the individual load components is correct. The negative phase difference, which is only a small fraction of the time required for the waves to reach the moored ship ($\sim 4\%$), cannot be explained by the error in the numerical wave celerity. Although the actual reason remains unclear, we hypothesise that this time shift (or spatial shift)[3] is related to a difference between the position of the ship in the laboratory and in the numerical model, and the relatively coarse schematisation of the hull (e.g., the bulbous bow is excluded in the model).However, the model reproduced the global arrival time of the waves at the ship as the load signals become non-zero at approximately the same moment in time (Fig C.1d-i). Furthermore, the model captured the order of magnitude and the periodicity of the individual load components, including their mutual dependence (e.g., $M_x' \ll M_y'$, and $M_y' \sim M_z'$).

Appendix C.2. Harbour basin

In HBr, the ship which is moored inside the rectangular harbour basin is subject to the same monochromatic wave as in OWr. Near the wavemaker, the predicted surface elevation signal compares well with the measurements for $t < 25$ s, when the (progressive) wave field at the sensors was not yet disturbed by the waves reflected at the gravel slopes in front of the harbour walls, the wave guides, and the wavemaker (Fig. C.2a). For $t > 25$ s, the predicted and observed signal became relatively stationary and the wave height is consistently over predicted (likely due to differences in the wave damping that is induced by the gravel slopes located in front of the harbour walls).

---

[3]A time shift of 0.35 s is equivalent to a wave propagation distance of ~ 0.4 m

Near the harbour entrance and inside the harbour basin, a (partially) standing wave field occurred due to wave reflections at the harbour walls and wave guides. Here, the conditions became approximately stationary for $t > 80$ s (see Fig. C.2b-i). Near the harbour entrance at sensor 4, the predicted wave field differs in magnitude and phase compared to the measurements (Fig. C.2b), whereas the predicted wave field agrees well at sensor 6 which is located inside the harbour (Fig. C.2c). On average, the discrepancies in the predicted wave field are larger compared to the results of OWr. This is likely due to the increased complexity of the conditions in subset HB due to the partial reflections at the gravel slopes and the occurrence of a standing wave field inside the harbour. Differences between the physical and numerical domain (e.g., due to the discretisation of the harbour) and small errors in the numerical phase velocity may not only result in phase differences, but also in amplitude differences between the predicted and observed wave field (possibly explaining the differences observed at sensor 4).
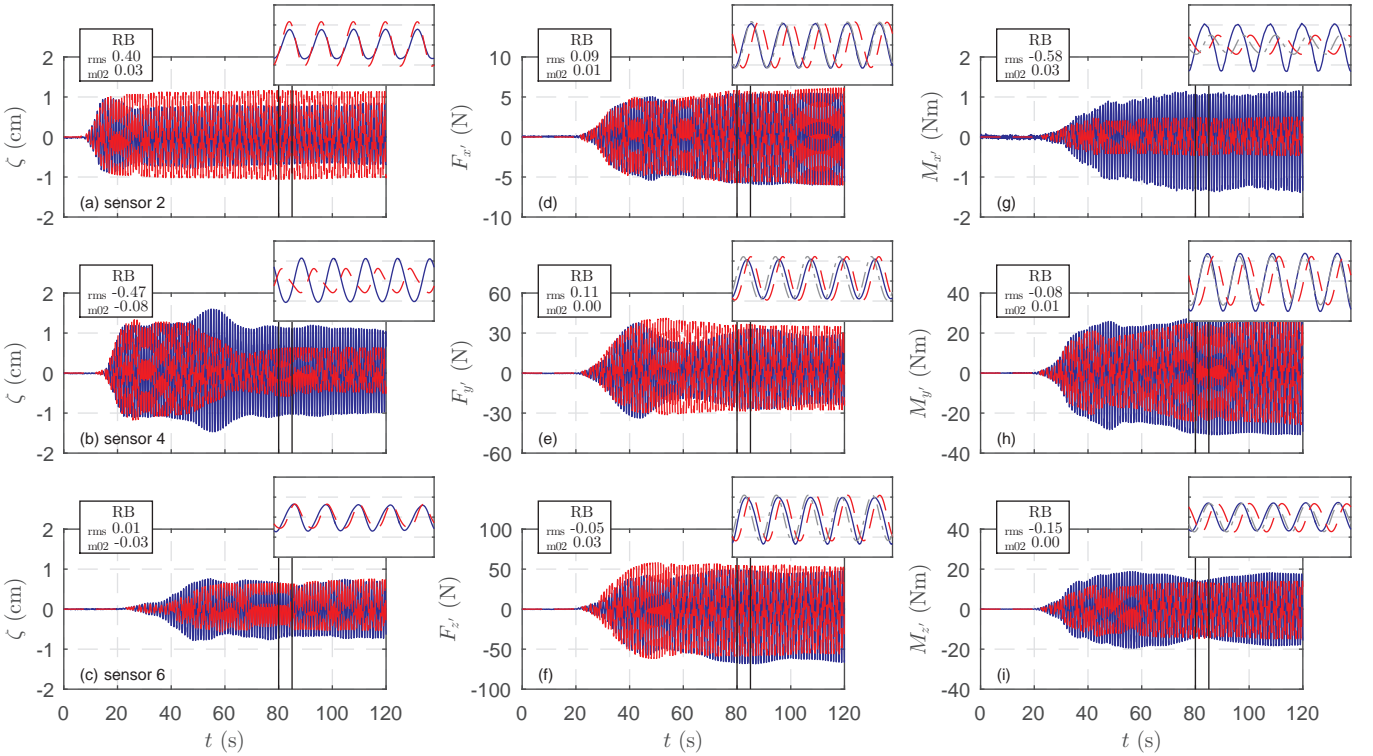

Figure C.2: Predicted (dashed red line) and observed (blue line) time series of the surface elevation ζ (a-c), and the forces F (d-f) and moments M acting on the ship (g-i) for HBr. The insets adjacent to the main panels show a close up of the results for $80 \leq t \leq 85$ s (illustrated by the two vertical black lines in the main panels). To facilitate a comparison between the predicted and observed hydrodynamic load signals, the dash-dot gray line in the insets of (d-i) shows the predicted hydrodynamic load signal including a time shift of -0.23 s. In each panel, the relative bias (RB) of the two bulk parameters are depicted in the top left corner. For brevity, the bulk wave heights and loads are denoted with $_{\mathrm{rms}}$, and the mean wave and load periods are denoted with $_{\mathrm{m02}}$. Note that in this case the scatter index is equal to the absolute value of RB.

36

The wave field near the harbour entrance (sensor 4) and inside the harbour basin (sensor 6), and the wave-induced loads acting on the moored ship became approximately stationary after $t > 60$ s (Fig. C.2b-i).

Despite the errors in the predicted wave field inside the harbour, the model reproduced the forces and moments that act on the ship (Fig. C.2d-i); except for M'_x, and a phase difference between the measured and predicted load signals. Similar to OWr, a constant time shift approximately corrects for the phase difference of all individual load components but $M_{x'}$. The errors in $M_{x'}$ suggest that relatively small discrepancies in the force components (in this case, $|RB| \leq 0.11$ for F'_y and F'_z) can cause significant discrepancies in the moment ($|RB| \leq 0.58$ for M'_x).

References

Barrett, R., Berry, M.W., Chan, T.F., Demmel, J., Donato, J., Dongarra, J., Eijkhout, V., Pozo, R., Romine, C., van der Vorst, H., 1994. Templates for the Solution of Linear Systems: Building Blocks for Iterative Methods. SIAM, Philadelphia.

Bertram, V., 2012. Practical Ship Hydrodynamics. Elsevier.

Bijleveld, H.J.M., 2004. Projectbeschrijving R&D Haves EZ-LIP: H3896.40 Validatie golfkrachten op schepen. Technical Report. WL — Delft Hydraulics.

Bingham, H.B., 2000. A hybrid Boussinesq-panel method for predicting the motion of a moored ship. Coastal Engineering 40, 21–38.

Bouscasse, B., Colagrossi, A., Marrone, S., Antuono, M., 2013. Nonlinear water wave interaction with floating bodies in SPH. Journal of Fluids and Structures 42, 112–129.

Brugnano, L., Casulli, V., 2009. Iterative solution of piecewise linear systems and applications to flows in porous media. SIAM Journal on Scientific Computing 31, 1858–1873.

Casulli, V., Stelling, G.S., 1998. Numerical simulation of 3D quasi-hydrostatic, free-surface flows. Journal of Hydraulic Engineering 124, 678–686.

Casulli, V., Stelling, G.S., 2013. A semi-implicit numerical model for urban drainage systems. International Journal for Numerical Methods in Fluids 73, 600–614.

Chorin, A.J., 1968. Numerical solution of the Navier-Stokes equations. Mathematics of Computation 22, 745–745.

Cointe, R., Geyer, P., King, B., Molin, B., Tramoni, M., 1991. Nonlinear and linear motions of a rectangular barge in a perfect fluid, in: Naval Hydrodynamics Proceedings, NAP. pp. 85–99.

Cui, H., Pietrzak, J.D., Stelling, G.S., 2012. Improved efficiency of a non-hydrostatic, unstructured grid, finite volume model. Ocean Modelling 54-55, 55–67.

De Bakker, A.T.M., Tissier, M.F.S., Ruessink, B.G., 2016. Beach steepness effects on nonlinear infragravity-wave interactions: A numerical study. Journal of Geophysical Research: Oceans 121, 554–570.

Dobrochinski, J.P.H., 2014. A combination of SWASH and Harberth to compute wave forces on moored ships. M.sc. thesis. Delft University of Technology.

González-Marco, D., Sierra, J.P., Fernández de Ybarra, O., Sánchez-Arcilla, A., 2008. Implications of long waves in harbor management: The Gijón port case study. Ocean & Coastal Management 51, 180–201.

Hadžić, I., Hennig, J., Perić, M., Xing-Kaeding, Y., 2005. Computation of flow-induced motion of floating bodies. Applied Mathematical Modelling 29, 1196–1210.

Hess, J.L., Smith, A.M., 1962. Calculation of non-lifting potential flow about arbitrary three-dimensional bodies. Technical Report. Douglas Aircraft Division. Long Beach, California.

865 Higuera, P., Lara, J.L., Losada, I.J., 2014. Three-dimensional interaction of waves and porous coastal structures using Open-

866   FOAM. Part I: Formulation and validation. Coastal Engineering 83, 243–258.

867 Holthuijsen, L.H., 2007. Waves in oceanic and coastal waters. Cambridge University Press.

868 Huijsmans, R.H.M., Pinkster, J.A., de Wilde, J.J., 2001. Diffraction and radiation of waves around side-by-side moored vessels,

869   in: The Eleventh International Offshore and Polar Engineering Conference, ISOPE.

870 Jacobsen, N.G., Van Gent, M.R.A., Wolters, G., 2015. Numerical analysis of the interaction of irregular waves with two

871   dimensional permeable coastal structures. Coastal Engineering 102, 13–29.

872 Jiang, T., Henn, R., Sharma, S.D., 2002. Wash waves generated by ships moving on fairways of varying topography, in: 24th

873   Symposium on Naval Hydrodynamics, NAP. pp. 8–13.

874 Korvin-Kroukovsky, B.V., Jacobs, W.R., 1957. Pitching and heaving motions of a ship in regular waves. Transactions of The

875   Society of Naval Architects and Marine Engineers 65, 590–632.

876 Lam, D.C.L., Simpson, R.B., 1976. Centered differencing and the box scheme for diffusion convection problems. Journal of

877   Computational Physics 22, 486–500.

878 Lin, P., 2006. A multiple-layer σ-coordinate model for simulation of wavestructure interaction. Computers & Fluids 35, 147–167.

879 Lin, P., 2007. A fixed-grid model for simulation of a moving body in free surface flows. Computers & Fluids 36, 549–561.

880 López, M., Iglesias, G., 2014. Long wave effects on a vessel at berth. Applied Ocean Research 47, 63–72.

881 Ma, G., Shi, F., Hsiao, S.C., Wu, Y.T., 2014a. Non-hydrostatic modeling of wave interactions with porous structures. Coastal

882   Engineering 91, 84–98.

883 Ma, G., Shi, F., Kirby, J.T., 2012. Shock-capturing non-hydrostatic model for fully dispersive surface wave processes. Ocean

884   Modelling 43-44, 22–35.

885 Ma, G., Su, S.F., Liu, S., Chu, J.C., 2014b. Numerical simulation of infragravity waves in fringing reefs using a shock-capturing

886   non-hydrostatic model. Ocean Engineering 85, 54–64.

887 Ma, Q.W., Yan, S., 2009. QALE-FEM for numerical modelling of non-linear interaction between 3D moored floating bodies

888   and steep waves. International Journal for Numerical Methods in Engineering 78, 713–756.

889 Madsen, P.A., 1983. Wave reflection from a vertical permeable wave absorber. Coastal Engineering 7, 381–396.

890 Mofidi, A., Carrica, P.M., 2014. Simulations of zigzag maneuvers for a container ship with direct moving rudder and propeller.

891   Computers & Fluids 96, 191–203.

892 Newman, J.N., 1977. Marine hydrodynamics. MIT press.

893 Newman, J.N., 2005. Efficient hydrodynamic analysis of very large floating structures. Marine Structures 18, 169–180.

894 Ren, B., He, M., Dong, P., Wen, H., 2015. Nonlinear simulations of wave-induced motions of a freely floating body using

895   WCSPH method. Applied Ocean Research 50, 1–12.

896 Rijnsdorp, D.P., Ruessink, G., Zijlema, M., 2015. Infragravity-wave dynamics in a barred coastal region, a numerical study.

897   Journal of Geophysical Research: Oceans 120, 4068–4089.

898 Rijnsdorp, D.P., Smit, P.B., Zijlema, M., 2014. Non-hydrostatic modelling of infragravity waves under laboratory conditions.

899   Coastal Engineering 85, 30–42.

900 Sakakibara, S., Kubo, M., 2008. Characteristics of low-frequency motions of ships moored inside ports and harbors on the basis

901   of field observations. Marine Structures 21, 196–223.

902 Smagorinsky, J., 1963. General circulation experiments with the primitive equations. Monthly Weather Review 91, 99–164.

903 Smit, P., Janssen, T., Holthuijsen, L., Smith, J., 2014. Non-hydrostatic modeling of surf zone wave dynamics. Coastal

904   Engineering 83, 36–48.

905 Smit, P., Zijlema, M., Stelling, G., 2013. Depth-induced wave breaking in a non-hydrostatic, near-shore wave model. Coastal

906   Engineering 76, 1–16.

907 Stansby, P.K., Zhou, J.G., 1998. Shallow-water flow solver with non-hydrostatic pressure: 2D vertical plane problems. Inter-

national Journal for Numerical Methods in Fluids 28, 541–563.

Stelling, G., Zijlema, M., 2003. An accurate and efficient finite-difference algorithm for non-hydrostatic free-surface flow with application to wave propagation. International Journal for Numerical Methods in Fluids 43, 1–23.

Stern, F., Yang, J., Wang, Z., Sadat-Hosseini, H., Mousaviraad, M., Bhushan, S., Xing, T., 2013. Computational ship hydrodynamics: Nowadays and way forward. International Shipbuilding Progress 60, 3–105.

Van der Molen, W., 2006. Behaviour of moored ships in harbours. Ph.D. thesis. Delft University of Technology.

Van der Molen, W., Monardez, P., Van Dongeren, A., 2006. Numerical simulation of long-period waves and ship motions in Tomakomai port, Japan. Coastal Engineering Journal 48, 59–79.

Van der Molen, W., Wenneker, I., 2008. Time-domain calculation of moored ship motions in nonlinear waves. Coastal Engineering 55, 409–422.

Van Kan, J., 1986. A second-order accurate pressure-correction scheme for viscous incompressible flow. SIAM Journal on Scientific and Statistical Computing 7, 870–891.

Van Leer, B., 1979. Towards the ultimate conservative difference scheme. V. A second-order sequel to Godunov's method. Journal of Computational Physics 32, 101–136.

Van Oortmerssen, G., 1976. The motions of a ship in shallow water. Ocean Engineering 3, 221–255.

Vitousek, S., Fringer, O.B., 2013. Stability and consistency of nonhydrostatic free-surface models using the semi-implicit θ-method. International Journal for Numerical Methods in Fluids 72, 550–582.

Wang, D.G., Zou, Z.L., Tham, L.G., 2011. A 3-D time-domain coupled model for nonlinear waves acting on a box-shaped ship fixed in a harbor. China Ocean Engineering 25, 441–456.

Wilson, R.V., Carrica, P.M., Stern, F., 2006. Unsteady RANS method for ship motions with application to roll for a surface combatant. Computers & Fluids 35, 501–524.

Xiong, L., Lu, H., Yang, J., Zhao, W., 2015. Motion responses of a moored barge in shallow water. Ocean Engineering 97, 207–217.

Yamazaki, Y., Kowalik, Z., Cheung, K.F., 2009. Depth-integrated, non-hydrostatic model for wave breaking and run-up. International Journal for Numerical Methods in Fluids 61, 473–497.

Yan, S., Ma, Q., 2007. Numerical simulation of fully nonlinear interaction between steep waves and 2D floating bodies using the QALE-FEM method. Journal of Computational Physics 221, 666–692.

You, J., Faltinsen, O.M., 2015. A numerical investigation of second-order difference-frequency forces and motions of a moored ship in shallow water. Journal of Ocean Engineering and Marine Energy 1, 157–179.

Zhao, W.H., Yang, J.M., Hu, Z.Q., Wei, Y.F., 2011. Recent developments on the hydrodynamics of floating liquid natural gas (FLNG). Ocean Engineering 38, 1555–1567.

Zijlema, M., Stelling, G., Smit, P., 2011. SWASH: An operational public domain code for simulating wave fields and rapidly varied flows in coastal waters. Coastal Engineering 58, 992–1012.

Zijlema, M., Stelling, G.S., 2005. Further experiences with computing non-hydrostatic free-surface flows involving water waves. International Journal for Numerical Methods in Fluids 48, 169–197.

Zijlema, M., Stelling, G.S., 2008. Efficient computation of surf zone waves using the nonlinear shallow water equations with non-hydrostatic pressure. Coastal Engineering 55, 780–790.